Correspondence to:

X.-M. Hu,
xhu@ou.edu

Author Contributions:

Conceptualization: Xiao-Ming Hu
Data curation: Xiao-Ming Hu, Wesley T. Honeycutt
Methodology: Xiao-Ming Hu
Resources: Binbin Weng, Ming Xue
Writing – original draft: Xiao-Ming Hu
Writing – review & editing: Chenghao Wang, Bowen Zhou

Observation and Simulation of Methane Plumes During the Morning Boundary Layer Transition

Xiao-Ming Hu[1,2] , Wesley T. Honeycutt[3] , Chenghao Wang[2,4] , Binbin Weng[3] , Bowen Zhou[5] , and Ming Xue[1,2]

[1]Center for Analysis and Prediction of Storms, University of Oklahoma, Norman, OK, USA, [2]School of Meteorology, University of Oklahoma, Norman, OK, USA, [3]School of Electrical & Computer Engineering, University of Oklahoma, Norman, OK, USA, [4]Department of Geography and Environmental Sustainability, University of Oklahoma, Norman, OK, USA, [5]School of Atmospheric Sciences, Nanjing University, Nanjing, China

Abstract Methane (CH_4) contributes significantly to global warming. However, accurate identification of CH_4 sources for reducing CH_4 emissions is often hampered by inadequate accuracy and spatiotemporal coverage of CH_4 detection, and lack of accurate CH_4 forward modeling used in top-down inversion systems. In this study, a field experiment was conducted in Pampa, Texas using two CH_4 sensors (LI-COR and OGI camera) to detect CH_4 releases. We investigated whether high-resolution simulations using the Weather Research and Forecasting (WRF) model with greenhouse gases (WRF-GHG) could accurately simulate the CH_4 plumes in the presence of evolving atmospheric boundary layer from sunrise to noon. CH_4 plumes showed substantial variation in time. At a release rate of $\sim 17.5 \, kg \, hr^{-1}$, the maximum enhancement of CH_4 measured by LI-COR was 2.6 ppm at sunrise (7:36 a.m.), 250 m from the release location. Within half an hour after sunrise, this enhancement decreased to 0.3–0.4 ppm. The enhancement was 0.2 ppm by 10:00 a.m. and further dropped to less than 0.1 ppm after 11:30 a.m. Due to the low temperature at sunrise, the OGI camera failed to detect the CH_4 plume. The WRF-GHG large-eddy simulation (LES) with 32 m grid spacing successfully reproduced these CH_4 enhancements. In situ measurements together with numerical simulations illustrate the impact of the transition from a stable boundary layer in the early morning to a convective boundary layer at noon on the dispersion of CH_4 plumes. Additionally, CH_4 plumes from a cattle farm in Oklahoma are briefly examined using the same modeling approach.

Plain Language Summary Methane (CH_4) contributes significantly to global warming. However, accurate identification of CH_4 sources for preventing/reducing CH_4 emissions is often hampered by the inadequate accuracy and spatiotemporal coverage of CH_4 detection, and the lack of accurate numerical modeling. In this study, a field experiment was conducted in Pampa, Texas using two CH_4 sensors (LI-COR 7810 and OGI camera) to detect controlled CH_4 releases. We investigated whether high-resolution simulations using the Weather Research and Forecasting (WRF) model with greenhouse gases (WRF-GHG) could accurately simulate the released CH_4 plumes in the presence of the evolving atmospheric processes from sunrise to noon. Despite changing atmospheric conditions, the WRF-GHG simulation with 32 m grid spacing successfully reproduced observed CH_4 enhancements. Measurements, together with numerical simulations, illustrate the impact of the transition of atmospheric processes on the variation of CH_4 plumes. Following the investigation of the Pampa case, WRF-GHG simulation is also applied to examine CH_4 plumes from a cattle farm in Oklahoma in a different season. This study illustrates that high-resolution WRF-GHG simulations can be used to understand CH_4 plume behavior under variable atmospheric conditions, providing guidance for quantifying CH_4 emissions from point sources.

1. Introduction

Methane (CH_4) is a potent greenhouse gas (GHG) that contributes significantly to global warming. It is responsible for around 30% of the effective radiative forcing from anthropogenic emissions of GHGs and their precursors and it accounts for $\sim 0.6°C$ increase in global surface air temperature during the industrial era (1750–2019) (IPCC, 2021). As one of the major sectors for CH_4 emissions, oil and gas industry was estimated to contribute around 56% or 67 Tg CH_4 of annual global anthropogenic CH_4 emissions during 2010–2019 in the latest global methane budget (Saunois et al., 2024). Ultra-emitters, short-term leak events with high CH_4 release ($>25 \, tons \, hr^{-1}$), could contribute an additional 8 Tg CH_4 annually (Lauvaux et al., 2022; Tibrewal et al., 2024).

Nevertheless, large uncertainties exist in the current estimation of these emissions on both regional and national scales (Chen et al., 2022; Saunois et al., 2020; Shen et al., 2023; Sherwin et al., 2024). This is mainly due to the lack of consistency in emission accounting methods and emission factors (Saunois et al., 2020).

Methane can be emitted both intentionally and unintentionally during the operation, maintenance, and system disruptions of the oil and gas industry. In addition to the potential climate and environmental benefits, reducing methane emissions can also bring significant economic values. A report by the ICF International (2014) estimated that a 40% reduction in CH_4 emissions from the U.S. onshore oil and gas industry could save up to $100 million annually. However, implementing emission reduction measures would cost $2.2 billion upfront. This highlights the challenges that the oil and gas industry are facing. Notably, approximately 30% of the U.S. domestic primary energy production is ensconced in the Southern Great Plains, including Texas and Oklahoma (U.S. EIA, 2023). Meanwhile, these states' economy depends heavily on energy production. For example, 8.2% of the employment in Oklahoma is directly related to energy extraction with the majority remaining non-farm jobs indirectly dependent on this industry (USEER, 2023). Oklahoma provides economic incentive to reduce methane emissions from these energy production operations. The average annual cost estimate for leak detection and repair for an oil and natural gas facility in the U.S. was estimated to be $191,075 in 2014 (ICF International, 2014), a sizable outlay for maintenance of equipment which is, ideally, remote. A reduction in monitoring frequency through targeted application of resources and/or refined accuracy through improved background monitoring would reduce this cost, and thereby reduce the barrier to attainment.

However, identification of CH_4 sources for preventing/reducing CH_4 emissions is often hampered by the lack of CH_4 detection with adequate accuracy and spatiotemporal coverage. CH_4 sensors are either too expensive for wide deployment to capture all possible CH_4 plumes or have too low precision to detect ambient CH_4 enhancements (Chen et al., 2024; Honeycutt et al., 2019, 2021; Riddick et al., 2022; Torres et al., 2022). Currently, the leak detection and repair (LDAR) protocols (U.S. EPA, 2014) rely heavily on optical gas imaging (OGI) cameras (Log et al., 2019; Lyman et al., 2019; Nutt et al., 2020; Safitri & Mannan, 2010; Stovern et al., 2020; Wang et al., 2020, 2022). While this technology is incredibly useful for identifying leak locations (Nisbet et al., 2020), it is limited to monitoring nearby CH_4 sources with a column density of the plume greater than 5,000 ppm-m when the temperature difference between gas and background is less than 2°C (Zeng & Morris, 2019). Additionally, it is incapable of quantitatively assessing the mass flow rates of leaks (Bergau et al., 2024). In addition, the operation of OGI cameras is subject to environmental conditions. Since OGI cameras require sunlight and temperature contrast with the background, they fail to work in nocturnal or low-temperature conditions. The coolness of the background scene persists in the morning during winter since it takes longer for the sun to heat the ground from overnight chills, which may lead to failure of OGI cameras (Zeng & Morris, 2019). As we shall see, these early morning conditions are the most ideal for evaluating emission plumes due to the shallow boundary layer. As research continues to address the unsolved question of the leaking rate that separate detectable from undetectable CH_4 sources using OGI cameras (Chen et al., 2024; Zeng & Morris, 2019), one purpose of this study is to examine CH_4 plume detectability by an OGI camera during morning transition periods.

CH_4 plumes are highly dictated by winds fields and atmospheric boundary layer (ABL) structure and associated turbulence fields. Given the same emission rate, CH_4 plumes may present significantly different characteristics (e.g., concentration and plume length) in different boundary layer conditions. During morning and evening transition hours, the boundary layer experiences profound changes (Acevedo & Fitzjarrald, 2001; Beare, 2008; Bonin et al., 2013; Lapworth, 2006), the impact of such changes on CH_4 plumes and the plume detectability remains largely unknown. Different boundary layer stability conditions and temperature profiles may result in different types of CH_4 plumes, such as fanning, looping, lofting, fumigating, or trapping (Arya, 1999; Hu et al., 2024; Stull, 1988). Assuming each of these conditions may happen under the same emission rate, an OGI camera observation occurring beyond the fence line at an oil and gas well pad emitting fugitive CH_4 may appear drastically different from the same observation point when operating under standard EPA Method 21 protocols (U.S. EPA, 2017), since the plume may be either dispersed or concentrated. Use of OGI detection is principally qualitative since attempting to quantify such a plume without necessary information about the boundary layer increases the likelihood of error. Therefore, over-reliance on OGI technology may not be ideal for inferring CH_4 emission rates. This study attempts to demonstrate a quantitative emission estimation method using highly accurate CH_4 concentration measurements and an atmospheric transport and dispersion model. Such a procedure is often referred to as top-down emission inversion because the goal is to deduce emission rate from observed

concentrations, in contrast to forward atmospheric modeling that predicts concentration based on known emission rates (Flesch et al., 2004). By establishing a connection that bridges the sensor–modeling gap, this approach offers an alternative to OGI-focused LDAR protocols.

In addition to measurement errors, CH_4 plumes in a changing boundary layer are hard to model accurately in forward transport model simulations, which would also prevent accurate top-down emission inversion (Chen et al., 2019; Feng et al., 2019a, 2019b). Top-down inversion systems determine the optimal emission rate to reconciling simulated and observed concentration fields using the emission–concentration relationship derived from forward simulations (Ciais et al., 2010; Flesch et al., 2004). Errors in simulating CH_4 plumes, though, can distort this relationship, introducing bias into CH_4 emission estimation. Some GHG gas inversion systems use the Gaussian plume model to derive emissions based on mobile or stationary measurements (Kumar et al., 2024; Pasquill, 1961), most notably the Other Test Method (OTM) 33A by the U.S. EPA (2014). However, the inverse Gaussian method poorly considers the dynamic plume response to ABL processes because the Gaussian plume model assumes a uniform flow with homogeneous and stationary turbulence, which is rarely the case in a real atmosphere (Arya, 1999; Wyngaard, 2010). Numerical weather prediction (NWP)-based GHG modeling provides a promising alternative to simulate GHG plumes in real atmospheric environments. The Weather Research and Forecasting model with Chemistry (WRF-Chem) is often used for regional simulation of GHGs using grid spacings of a few km or sub-km (Barkley et al., 2023; Hu, Gourdji, et al., 2021; Ye et al., 2020; Zhao et al., 2019, 2023). These simulations often use GHG emissions aggregated in grid cells as coarse as km-scales based on bottom-up inventories, and they can only simulate GHG plumes at urban/basin scales. Fugitive/vented emissions from single points are often not available from inventory data. Thus, conventional WRF-Chem simulations cannot resolve CH_4 plumes from individual sites, which may only spread/span for a few kilometers or even a few hundred meters and occur every few kilometers, let alone individual wells spaced a few meters apart in modern horizontally drilled facilities. The lack of high-resolution NWP-based simulation of fugitive plumes is partly due to the lack of ground-based measurements for model validation. Most in situ GHG measurement networks are designed to measure aggregated urban emissions rather than individual plumes. Therefore, the relevant research questions include: Can high-resolution NWP-based models be used for modeling fugitive emissions? Can they reproduce the impact of ABL turbulence on plumes? Which sensing techniques can detect GHG plumes for model evaluation?

Large-eddy simulations (LESs) operating on $\mathcal{O}$ (1–10 m) spatial resolutions can explicitly resolve the large energetic eddies in the ABL, and have been used to simulate turbulent dispersion of scalar plumes dating back to early works of 1990s (Nieuwstadt, 1992a, 1992b). Recently, LES has been applied to quantifying uncertainties associated with atmospheric variability in CH_4 field measurements and to provide guidance for observation strategies (Caulton et al., 2018; Delkash et al., 2016; Raznjevic et al., 2022; Taylor et al., 2016). Notably, Caulton et al. (2018) used LES to analyze uncertainties in the estimated CH_4 emissions derived from inverse Gaussian methods based on vehicle-mounted measurements, and suggested a hierarchical sampling strategy for mobile transects. Along a similar line of investigation, Raznjevic et al. (2022) used LES to evaluate EPA's OTM 33A that relies on applying inverse Gaussian estimation based on downwind point measurements, and quantified uncertainties associated with the Gaussian model, wind-shear effects, and mis-alignment of plume and measurement heights. However, both studies considered only neutral conditions, while the effects of stratification on ABL turbulence were not accounted for.

In this study, a field experiment in Pampa, Texas was conducted using two CH_4 sensors (LI-COR 7810 and OGI camera) to detect controlled CH_4 releases. We investigated whether high-resolution simulations using the WRF model with greenhouse gases (WRF-GHG) could accurately simulate the released CH_4 plumes in the presence of the evolving boundary layer structure from sunrise to noon. We applied WRF-GHG at a very high spatial resolution of tens of meters, essentially operating the model in LES mode (WRF-GHG LES). While this approach is widely used in idealized studies of atmospheric turbulence it is rarely used in GHG research for simulating actual plume dispersion over real terrain. The in situ ground-truth measurements from the Pampa experiment provide an opportunity for evaluating the LESs, and such LESs are used to examine the dynamics of CH_4 plumes in the ABL from sunrise to noon. To further validate the generalizability of this approach, we applied the WRF-GHG LES to examine CH_4 plumes from a cattle farm in Oklahoma during a different season.

2. Model Description, Configuration, and Field Experiment

2.1. WRF-GHG Model Configurations for Large-Eddy Simulation (LES) of CH_4

In our previous work (Dong et al., 2021; Hu et al., 2020, 2021a; Li et al., 2020, 2023), the WRF-VPRM, a weather-biosphere-online-coupled model (Ahmadov et al., 2007) in which the biogenic CO_2 fluxes are handled by the Vegetation Photosynthesis and Respiration Model (VPRM, Mahadevan et al., 2008; Xiao et al., 2004), has been improved and applied to examine CO_2 fluxes and concentrations at regional scales. In this work, an enhanced version of the WRF-VPRM by including CH_4 (referred to as WRF-GHG hereafter) was further developed by coupling with the Copernicus Atmosphere Monitoring Service (CAMS) CH_4 global simulation for the initial and boundary conditions and ingesting the WetCHARTs wetland CH_4 emissions (Bloom et al., 2017) and anthropogenic CH_4 emissions (Francoeur et al., 2021; Gorchov Negron et al., 2018). WRF-GHG has been shown to capture the monthly variation of CO_2 and CH_4 concentrations, as well as their episodic variations associated with frontal passages over the United States. The simulation results are validated using multiple data sets, including remotely sensed data from Total Carbon Column Observing Network (TCCON), OCO-2, TROPOMI, and in situ measurements from the GLOBALVIEW obspack data (Hu, Xue, et al., 2021).

To guide the field experiment at the Pampa site (described in Section 2.2) and to examine the impact of meteorology on CH_4 plumes during the field experiment, a quadruply nested WRF-GHG domain was set up with sequentially refined grid spacing, that is, 12 to 0.8 km to 0.16 km and to 32 m. The outermost domain covers the contiguous United States, the second domain covers the Texas panhandle region, while the third and the fourth domain zoom-in on the Pampa site. Only the first two domains were activated for real-time forecasting to guide the field experiment, and all 4 domains were activated for detailed retrospective LES of CH_4. Land elevations were taken from the Shuttle Radar Topography Mission (SRTM) data at a resolution of 1 arc-second (30 m). Figure 1 shows the land elevations in the innermost domain. Two land use data sets were used: the MODIS land use with a 1 km resolution and the National Land Cover Database (NLCD) with a 30 m resolution. The higher-resolution NLCD land use leads to a smoother temperature field in the early morning, while its impact on flow dynamics and CH_4 plume behavior at the research site in the presence of southerly winds is minimal (figure not shown). Therefore, only the NLCD results are presented in the following sections. The model domain has 47 vertical layers extending from the surface to 10 hPa with 21 layers in the lower 2 km above the ground to resolve boundary layer processes. The operational Global Forecast System (GFS) 0.25-degree-resolution data provided meteorological initial and boundary conditions and the CAMS $3° \times 2°$ global inversion-optimized concentrations provided initial and boundary conditions for CH_4 (Segers & Nanni, 2024). Anthropogenic CH_4 emissions were taken from the 4×4 km Fuel-based Oil and Gas (FOG) Inventory (Francoeur et al., 2021; Gorchov Negron et al., 2018). The CAMS initial and boundary CH_4 conditions and the coarse FOG emissions provided the background CH_4 concentration. A CH_4 emission rate of 17.5 kg hr^{-1} was added at the Pampa site based on the CH_4 controlled release rate, which varied by only 2% on the morning of the field experiment day (28 Mar. 2024). CH_4 plume from this point source is the focus of this study. While the CH_4 emission rate is applied through the whole simulation period, the actual controlled release occurred randomly (Figure 2).

Selected major physics parameterization schemes within WRF-GHG include the Dudhia shortwave radiation scheme (Dudhia, 1989), the rapid radiative transfer model (RRTM) (Mlawer et al., 1997) for longwave radiation, the Noah land surface model (Chen & Dudhia, 2001), and the Shin-Hong planetary boundary layer (PBL) scheme (Shin & Hong, 2015). Selection of PBL schemes is critical for accurate simulation of lower tropospheric CH_4 vertical distribution (Ballav et al., 2016; Diaz-Isaac et al., 2018; Hu et al., 2012). The Shin-Hong scheme is a scale-aware nonlocal scheme with explicit treatment of entrainment fluxes, which has been shown to be critical to reproducing boundary layer structures (Hu et al., 2019a). The Shin-Hong scheme adopts a nonlocal heat flux profile fitted to LES results, and achieves scale-awareness (or horizontal grid spacing dependency) through scaling both local and nonlocal eddy fluxes according to the normalized grid spacing (Shin & Hong, 2013). Since the third and the fourth model domains focusing on the Pampa site reach LES resolutions, PBL scheme was turned off and a 1.5 order three-dimensional turbulence kinetic energy (TKE) closure was used for subgrid-scale (SGS) mixing, following previous nested WRF-LES studies (Chu et al., 2014; Mirocha et al., 2013, 2014). Two additional sensitivity simulations were also conducted using the first-order Smagorinsky closure (Smagorinsky, 1993) and the scale-aware 3D-TKE scheme (Zhang et al., 2018) for SGS mixing. Since no precipitation occurred during the experiment, cumulus and microphysics schemes were deemed less relevant.
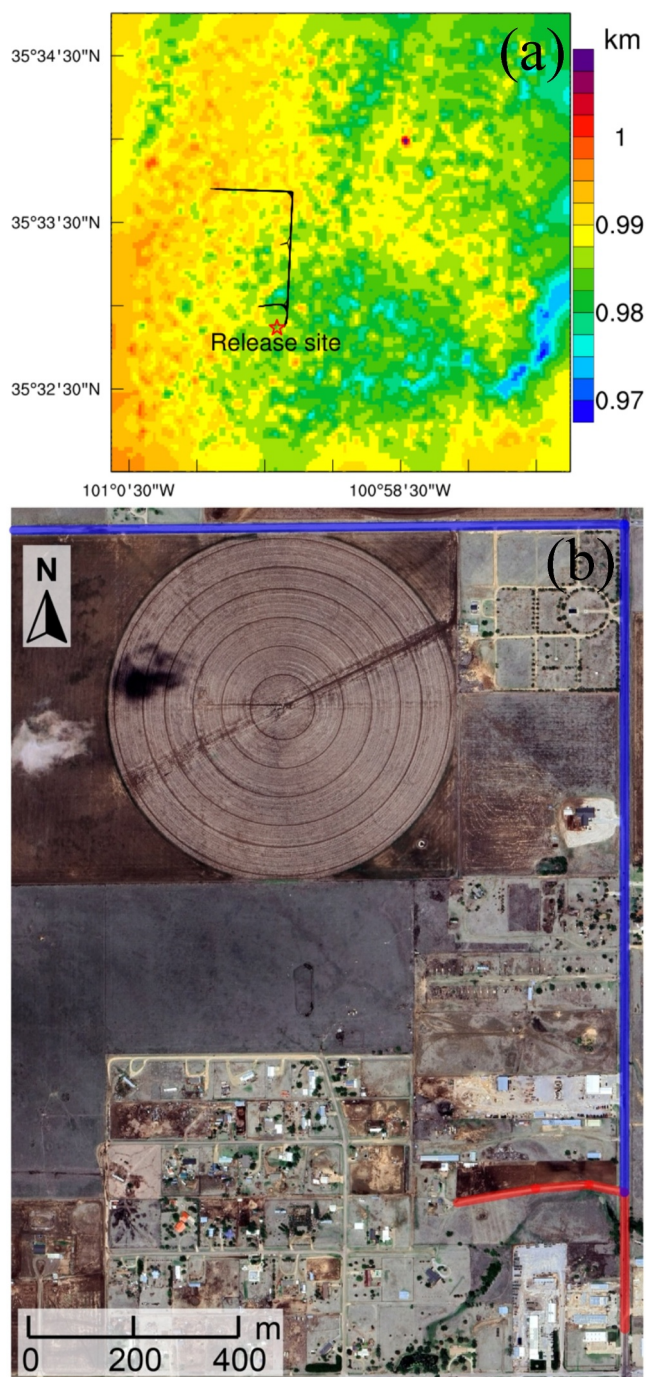
Figure 1. (a) Land elevations over the fourth domain, taken from the Shuttle Radar Topography Mission (SRTM) data at a resolution of 1 arc-second (30 m). The industry partner site and driving path are marked. (b) Satellite imagery (dated on 05/15/2023) of the experiment region with the driving path marked, including the short red route and long blue route, the west-east portion of which is 250 m and 1.45 km to the north of the site, respectively.

The WRF-GHG real-time forecasting with the outer two domains only was launched daily (posted at https://caps.ou.edu/micronet/WRF_GHG_Forecasting_Pampa.html) before the experiment. These forecasts were used to select a suitable day for measuring the CH_4 plume on the north side of the Pampa, TX site where we had access. Following the field experiment, nested WRF-GHG LES runs were conducted to examine CH_4 plumes within a changing boundary layer throughout the day. The fine horizontal and vertical resolutions used in this study can better resolve small-scale processes and the shallow surface layer, which is critical for accurately reproducing the formation of CH_4 plumes within a few hundred meters or kilometers under different conditions.

2.2. Field Experiment in Pampa, Texas

2.2.1. Field Site and Deployment Plan

A field experiment to measure controlled CH_4 release at a partner facility in Pampa, TX was planned. Such an experiment depends on the site availability, wind conditions, and other site-specific constraints. The WRF-GHG real-time forecasting was monitored daily to ensure the optimal weather and plume conditions, and 28 March 2024 was finalized as the experiment date. On this date, the Pampa facility performed controlled releases of natural gas to enable the evaluation of sensor technologies and WRF-GHG LES. A suite of instrumentation was deployed to measure the released CH_4 plumes. The emission site had a large southerly wind fetch with minor obstructions (single-story buildings) in other directions (see satellite image in Figure 1b). Instrument location and co-locations were determined during this field study for southerly wind conditions. Land access permissions were obtained from landowners to the north of the emission site prior to the experiment. A natural gas leak was simulated using a mass-flow metered release of natural gas from the Pampa, TX city supply. The volumetric CH_4 concentration of the natural gas source was reported as 87.56% by online gas chromatography at the release point. The maximum expected volumetric flow rate of gas from the emission source was 26.0 thousand cubic feet (MCF) day^{-1}. Our anonymous industry partners operating the site were given a randomized release schedule which varied the release pressure up to 15 psi from a 2" orifice, corresponding to a 30% change of the maximum flow rate. Gas was released in a single blind design, which meant that researchers operating sensors on routes did not know either the exact release timing or the pressure of the release.

2.2.2. Instruments in the Field

The field work was supported by a host of instruments available from both University of Oklahoma (OU) collaborators and industry partner resources. These included.

- A LI-COR 7810 in situ trace gas analyzer. This instrument was fitted with an inlet tube and filter. The inlet tube was placed outside the window of a Honda Odyssey van, just above the roofline, on the port side of the vehicle to sample gas acquired during motion from the slipstream of the vehicle. The vehicle was driven <10 mile hr^{-1}, where possible, to produce regular sampling. The vehicle was driven on areas with explicit landowner permission and public right-of-way only (see the routes in Figure 1).
- A Sierra Olympic Ventus optical gas imaging (OGI) camera mounted on a DJI Matrice 300 Unmanned Aircraft Systems (UAS) and a handheld camera used to visualize CH_4 plumes. The camera was operated by site personnel during the release to visualize plumes of gas emitted from the emission source. These
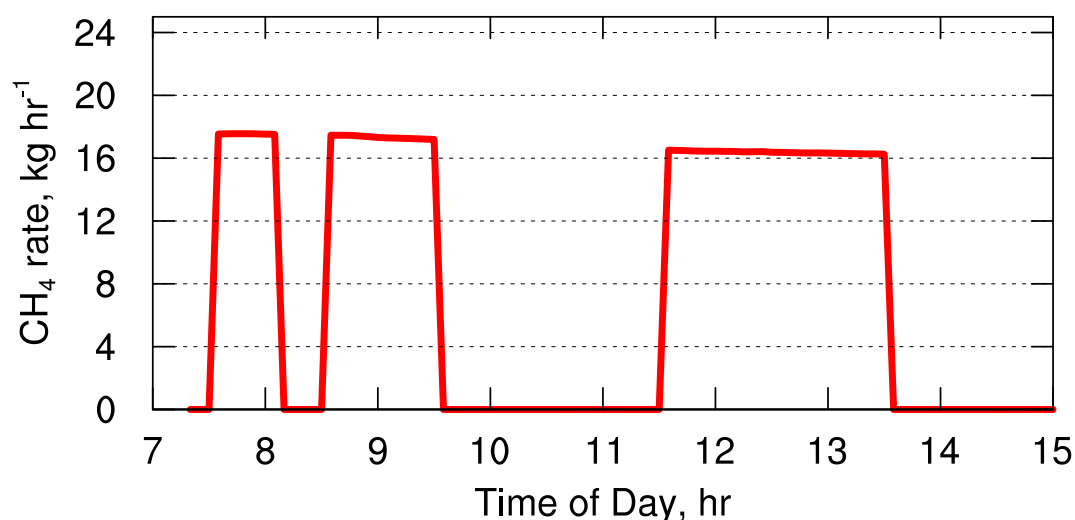
Figure 2. Controlled CH_4 release rate at the Pampa, TX site on 28 March 2024.

    observations confirmed that the LI-COR sensor was reporting emission enhancements due to gas produced by this leak. Videos from these flights were recorded by the site personnel. Videos were analyzed for gas concentration using Teledyne's quantitative OGI interface. Similar analysis technologies are reported in the literature with a median relative error of 24.4% at emission rates above 1 kg hr^{-1} (Bell et al., 2023).

- Meteorology at the release site was monitored using a Lufft WS500-UMB all-in-one meteorology sensor connected with a Campbell-Scientific CR6 logger. These instruments recorded 1-min samples and 5-min rolling average data. The all-in-one meteorology sensor was mounted 5 m above ground level. These meteorological data were used to evaluate WRF-GHG simulated surface temperature.

The LI-COR and meteorology sensors were operated by the OU team and the OGI camera was operated by the anonymous industry partners. The operational balloon soundings in Amarillo, TX (75 km to the southwest of the Pampa, TX) at 07:00 a.m. and 07:00 p.m. are also used to examine boundary layer structure and stability. Simulated winds are evaluated using the surface Mesonet data at Pampa (35.6 N, 100.98 W, ~6 km north to the CH_4 release site) archived by the Meteorological Assimilation Data Ingest System (MADIS).

Following the investigation of the Pampa case, a similar approach (mobile LI-COR 7810 measurement and WRF-GHG LES) was applied to examine the CH_4 plumes on 23 June 2024 from the Muegge cattle farm in Oklahoma, located ~6 km northwest of the Atmospheric Radiation Measurement (ARM) Southern Great Plains (SGP) atmospheric observatory site. The CH_4 plume from the cattle Farm is suspected to affect the ARM site occasionally during nighttime (Wang et al., 2024).

3. Results

During the field experiment, natural gas was released following a single-blind schedule such that the site operators knew the timing and flow rates of the release, but the OU measurement team did not. The measurement team anecdotally noted sudden changes in observed concentrations (e.g., alternating periods of apparent CH_4 enhancement and those with no detected enhancement), which aligned with changes in release rate revealed after the experiment. This indicates that the LI-COR sensor produced reasonable and reliable data during the experiment. For example, between 8:10 and 8:30 a.m. local time, no CH_4 enhancements were observed, which coincided with a pause in the controlled release (Figure 2).

The observed CH_4 enhancement varied significantly throughout the day. Note that the CH_4 plumes exhibited bell-shaped patterns, with the CH_4 enhancement defined as the increase in concentration above the background level at the edges of the bell shape. The enhancement at the short route (250 m north of the release site) decreased through our experiment from early morning to afternoon (Figures 3 and 4). On March 28, the sunrise time in Pampa was 7:36 a.m. At sunrise, we observed a peak concentration of 4.8 ppm, that is, an enhancement of 2.6 ppm over the background 2.2 ppm, during a transect from 7:36 to 7:41 a.m., and observed an enhancement of 0.4 ppm during
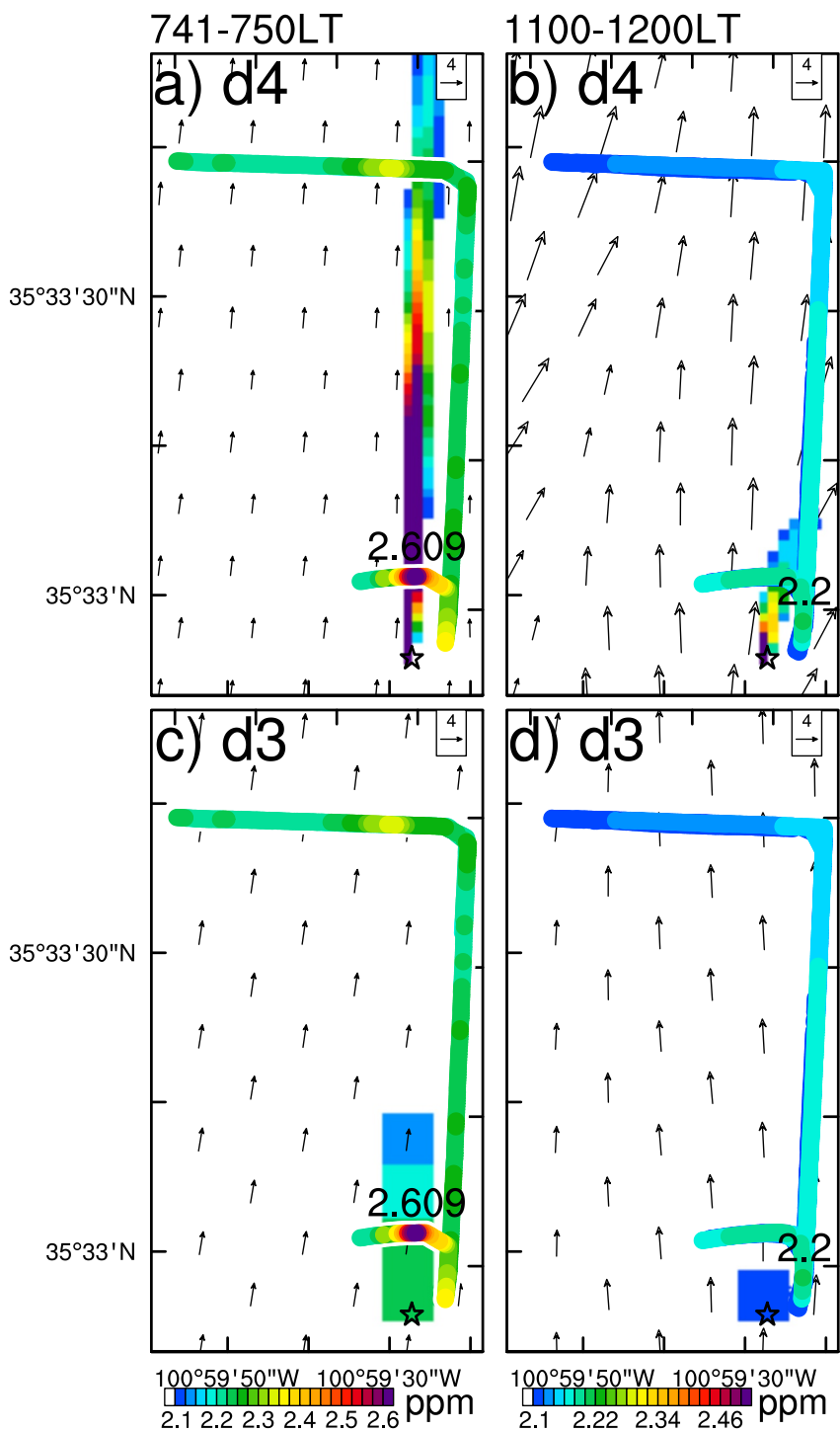
Figure 3. Simulated CH$_4$ mixing ratios and wind vectors (reference vector of 4 m s^{-1} marked in top-right corners) in domain (a), (b) 4 and (c), (d) 3 overlaid with observed mixing ratios along the driving routes during (left) sunrise and (right) noon time. The numbers are the observed maximum mixing ratios at the time period.

7:41–7:50 a.m. (Figures 3a and 4), corresponding to the coldest time of the day (Figure 5a). The enhancement at the short route decreased to 100 ppb through the course of the morning (Figure 4) and fell below 100 ppb between 11:00 a.m. and 12:00 p.m. (Figure 3b). After 12:30 p.m., the enhancement dropped to below 60 ppb. All these enhancements were recorded along the short route (~250 m from the release point). At the long route (1.5 km
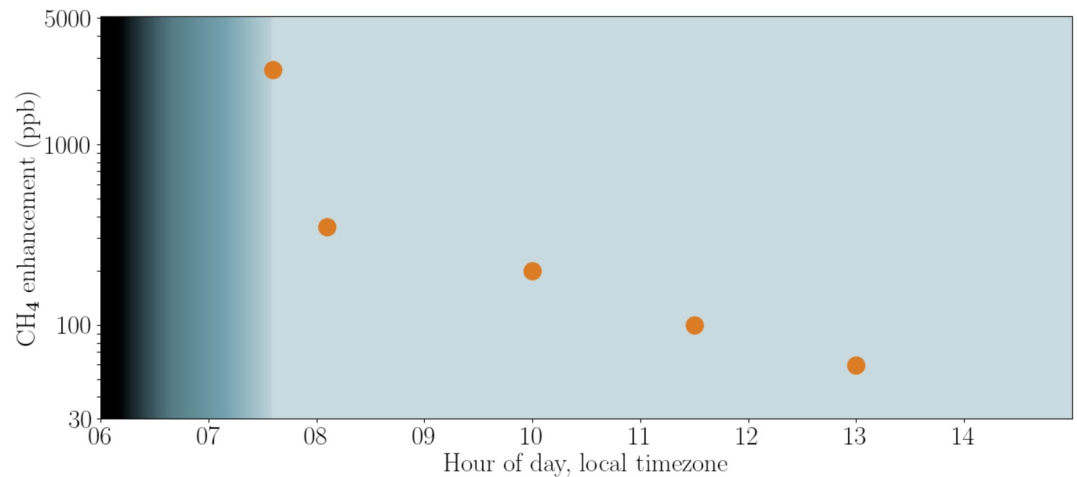
Figure 4. Time series of observed CH_4 enhancement at 250 m from the release. The color shade in the background depicts the twilight transition.

from the release location), we did not detect any significant enhancements, except a 100 ppb enhancement at 7:45 a.m. (section in light yellow on the northernmost leg of the long route in Figure 3a). Since the released plumes experienced the most substantial changes from sunrise to noon (Figure 4), the subsequent analyses will mainly focus on the CH_4 variation and the influential factors during this period.
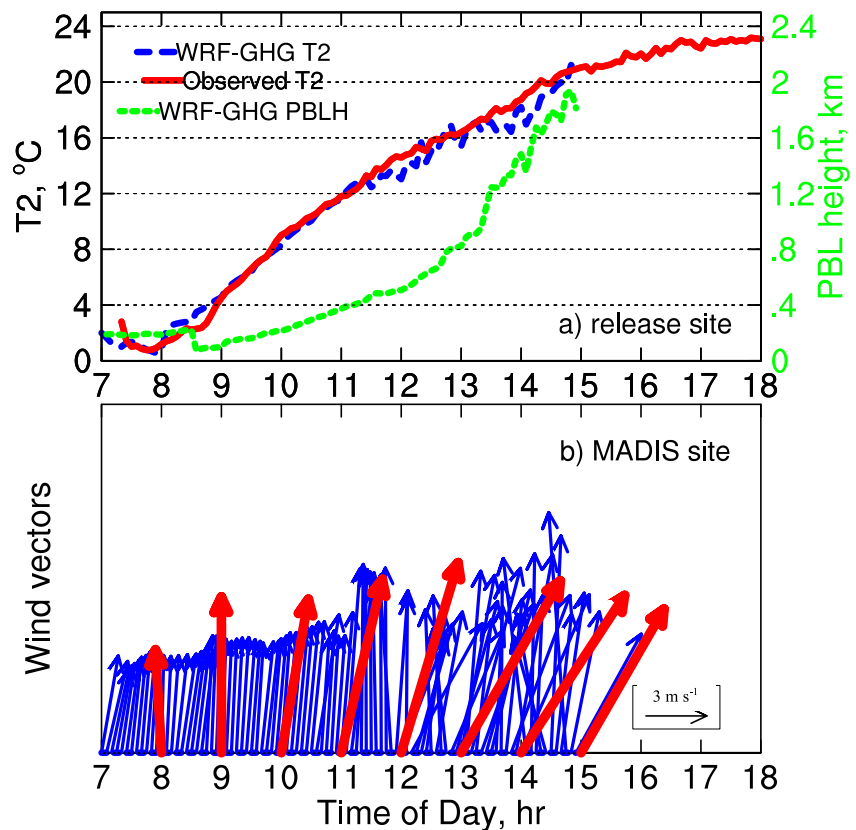
Figure 5. (a) Surface temperature at 2 m above the ground (T2) and simulated PBL height (PBLH) at the Pampa, TX site, and (b) wind vectors at the MADIS site in Pampa (35.6 N, 100.98 W) on 28 March 2024 observed and simulated in the inner most domain with LES configuration. A reference vector of 3 m s^{-1} is marked in panel (b). Note that while simulated T2 is instantaneous value, the observed T2 by the Lufft WS500-UMB all-in-one meteorology sensor is 5-min average.
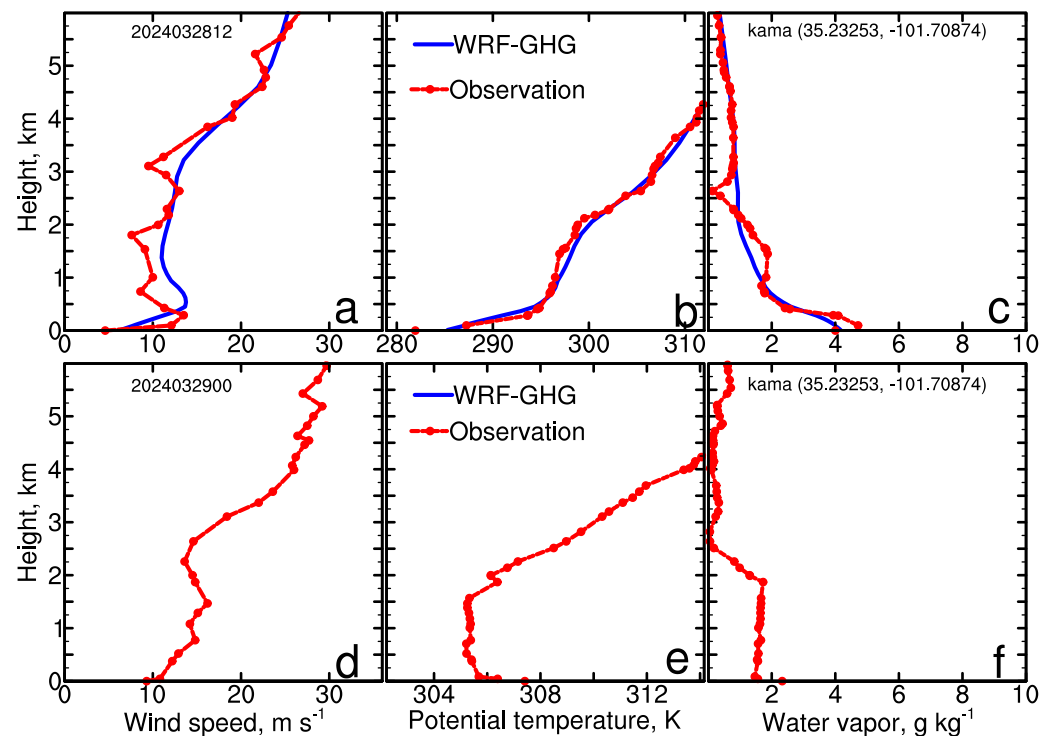
Figure 6. Observed and simulated profile of (a), (d) wind speed (b), (e) potential temperature (θ), and (c), (f) water vapor mixing ratio at Amarillo, TX (75 km to the southwest of the Pampa, TX site) at (top) 0700 and (bottom) 1900 local time on 28 March 2024. The WRF-GHG LES only runs up to 1500 local time, thus simulated profile at 1900 local time is not available.

The controlled CH_4 release before 1:30 p.m. maintained roughly the same rate when the release was turned on (Figure 2). CH_4 emission rate ranged between 17.56 and 17.19 kg hr^{-1} (only by 2%) during 7:35–9:30 a.m. (except during a brief pause from 8:10 to 8:30 a.m.). Thus, the significant variation in CH_4 concentrations (by two orders of magnitude, from ppm to tens of ppb) during each of our observation trips must have been dictated by atmospheric variability. The WRF-GHG LES in domain 4 with a grid spacing of 32 m generally reproduced the atmospheric flow characteristics of the site and the CH_4 plumes. Simulated CH_4 concentration at the ground level aligned well the concentrations and narrow plume widths (60–90 m) of the CH_4 plumes as observed by the LI-COR sensor from sunrise to noon (Figures 3a and 3b). This indicates the WRF-GHG model correctly captured the impact of boundary layer meteorology on CH_4 plumes as the ABL evolved throughout the day. In comparison, in domain 3 with a grid spacing of 160 m, the model could not resolve the measured plume at such close proximity and underestimated the plume enhancement by ~400 ppb at 7:50 a.m. (Figure 3c). In the grid cell containing the release point, the emission was diluted 25 times in a 160 m grid cell compared with a 32 m grid cell in domain 4, leading to this substantial underestimation. Thus, we will focus on the results of the WRF-GHG simulation in domain 4.

The measured surface temperature at the Pampa site, winds at the MADIS site in Pampa, and the balloon sounding in Amarillo, TX (75 km to the southwest of the Pampa, TX) were used to evaluate the lower tropospheric meteorology simulated by WRF-GHG (Figures 5 and 6). WRF-GHG reproduced the observed surface temperature quite well in domain 4 (Figure 5) with a mean bias of $-0.3°C$ (NMB of -2.4%) and underestimated surface wind speed by -17.1% (Table 1). These performance is comparable to operational NWP simulations (Hu et al., 2023). WRF-GHG simulation started integration at 7:00 a.m. After a half-hour spinup, the simulated surface temperature aligned well with observations after 7:30 a.m. However, the simulated temperature showed more variation than observations after 11:30 a.m., likely due to the impact of large turbulent eddies (as will be discussed later). Because WRF-GHG was run in LES mode with high resolution (a grid spacing of 32 m), the simulation was capable of resolving large turbulent eddies that are ubiquitous and random in the daytime convective boundary layer. These large eddies induce temperature variation (Gibbs & Fedorovich, 2014; Liu et al., 2018). The large air temperature variation and wind vector variation caused by individual large eddies were well resolved by the

Table 1

Evaluation Statistics for Simulated Temperature at 2 m AGL (T2) and Wind Speed Against Observations in Pampa on 28 March 2024 Following Our Previous Model Evaluation Practice (e.g., Hu et al., 2010; Hu et al., 2013; Hu, Xue, Kong, & Zhang, 2019; Hu, et al., 2021)

Metrics	T2 (°C)	Wind speed (m s^{-1})
Mean obs	11.4	8.3
Mean sim	11.1	6.9
r	0.996	0.689
MB	−0.3	−1.4
MAGE	0.6	1.6
RMSE	0.8	1.9
NMB	−2.4%	−17.1%

Note. The metrics include correlation coefficient *r*, mean bias (MB), mean absolute gross error (MAGE), root mean square error (RMSE), and normalized mean bias (NMB). Their formula can be found in Yu et al. (2006).

model (manifested in the instantaneous fields simulated by WRF-GHG) after 11:30 a.m. (Figure 5). In comparison, the observations were 5-min averages from the Lufft WS500-UMB meteorology sensor, so the variations due to large eddies were likely smoothed out. Thus, the time series of observed temperature appeared smoother than that of the simulated temperature.

In addition to the surface temperature, the atmospheric boundary structure/stability is examined in Figure 6. Potential temperature (θ) profiles provide a straightforward and meaningful representation of stability, with inversions representing stable conditions and decrease with height indicating unstable conditions (Hu et al., 2024). The simulated and observed profiles of wind speed, potential temperature, and water vapor mixing ratios in Amarillo, TX show an excellent agreement at 7:00 a.m., suggesting a very stable shallow boundary layer (∼200 m) where water vapor was confined (Figures 6a–6c). Twelve hours later at 7:00 p.m., a well-developed convective boundary layer was observed as shown by the balloon sounding, with the capping inversion (indicating boundary layer top) residing at ∼2 km above the ground (Figures 6d–6f). Consistent with observations, the simulated convective boundary layer height varies from 100 m in the early morning to ∼2 km in the afternoon (Figure 5a). Large turbulent eddies normally have scales resembling the boundary layer height. Thus, large eddies on this day should have scales of 1–2 km, as confirmed by WRF-GHG LES later. Note that routine operational soundings were available only twice a day.

The simulated boundary layer height increased over time except during a transition period around 8:30 a.m. from nighttime stable boundary layer to daytime convective boundary layer, when the boundary layer height appeared to collapse. This apparent collapse is deceiving and it is actually due to the different treatment of stable and convective boundary layers in the Shin-Hong PBL scheme and its predecessor, Yonsei University (YSU) scheme. In both schemes, a critical Richardson number of 0.25 is used to diagnose boundary layer height under stable conditions; while for unstable condition, a critical Richardson number of 0 is used (Hong, 2010; Hu et al., 2013). Thus the simulated "collapse" in the early morning transition actually indicates boundary layer growth from stable to convective boundary layer.

These boundary layer and turbulence variations dictate the dynamics of CH$_4$ plumes. Horizontal distributions and vertical cross-sections of simulated CH$_4$ plumes at 8 a.m. and 11:15 a.m. are compared in Figure 7, which are representative of early morning stable boundary layer and daytime convective boundary layer. During the early morning, the CH$_4$ plume was confined within a shallow layer near the surface and lengthily stretched downwind. There was an enhancement of about 100 ppb beyond 1.6 km (1 mile) from the release site. The CH$_4$ plume was barely dispersed vertically, limited by the high stability during the early morning as shown in the observed and simulated profiles (Figure 6) and the vertical cross-section of potential temperature (Figure 8c). Potential temperature shows a compact layered structure, indicating a very stable boundary layer and thus a very small vertical mixing coefficient (<1 m^2 s^{-1}, Figure 8a).

When approaching local noon, the surface CH$_4$ plume became shorter and was transported upwards about 300 m from the release site, driven by large turbulent eddies in the convective boundary layer. These large eddies can be clearly seen from the spatial distribution of temperature and vertical velocity (Figure 9). During the early morning, the temperature distribution exhibited a patchy pattern, reflecting the initial patchy distribution of land properties with a grid spacing of ∼1 km in the MODIS land use (figure not shown). This indicates that when turbulent eddies were not yet developed in the early morning, the surface temperature was primarily determined by the surface energy balance, which was dictated by land surface properties including land cover and soil properties. Using the higher-resolution National Land Cover Database (NLCD) land use, the patchy pattern disappeared (Figure 9a). Later at 11:15 a.m., the spatial distribution of temperature and winds was dominated by large eddies approximately 1 km wide in the west-east direction. Such a scale is comparable to the boundary layer height indicated by the afternoon sounding on this day (Figure 6). As the turbulent eddies actively developed, the spatial distribution of surface temperature and winds became less tied to land surface heterogeneity. Unlike the cellular structures under weak wind conditions (Gibbs & Fedorovich, 2014; Liu et al., 2018), the large eddies in our case manifest as elongated roll vortices likely due to strong surface winds (∼10 m s^{-1}, Figures 6a and 6d). The
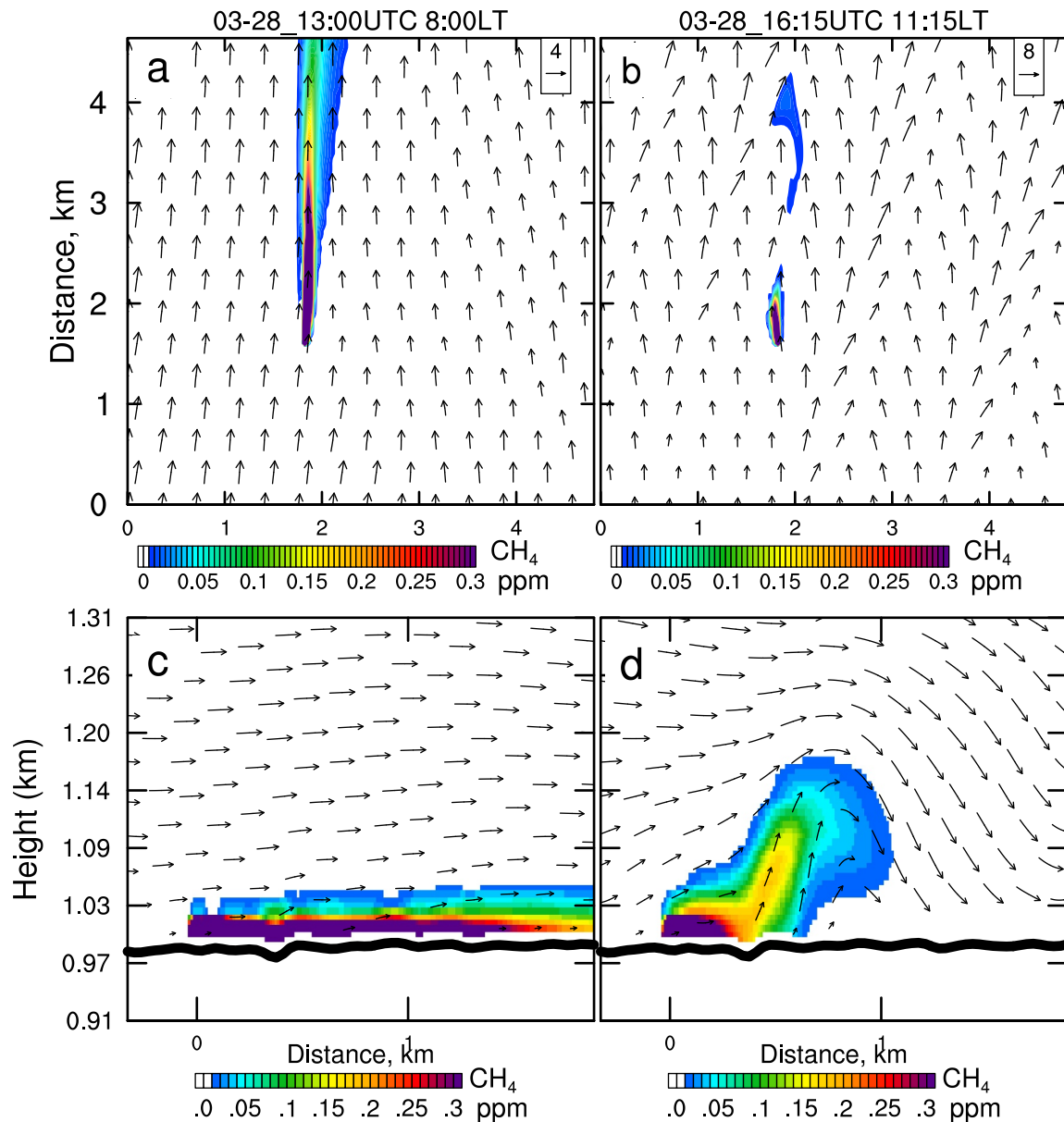
Figure 7. (a), (b) Horizontal spatial distribution and (c), (d) vertical cross-section of CH_4 enhancement plumes during (left) sunrise and (right) at local noon.

large eddies and flow streamlines follow potential temperature contours or isentropes as shown in vertical cross-sections (Figure 8d) given that potential temperature is conserved along air parcel trajectories when diabatic heating is negligible (Bluestein, 1992; Bonin et al., 2020; Smith, 1979; Xue & Thorpe, 1991).

Large eddies cause meandering of the CH_4 plumes in the mature daytime convective boundary layer (Figure 10). The CH_4 plume may be captured by a large eddy (as illustrated by spatial distributions of temperature and winds in Figure 11) at random distances from the release—for example, at 1 km at 11:30 a.m., 200 m at 11:45 a.m., or immediately from the release along an elongated convergency line at 12:35 p.m. (Figure 10). In addition, as indicated by the mixing coefficient (Figures 8a and 8b), SGS turbulence mixing was larger in the convective boundary layer around noon than early morning. Thus, the surface CH_4 plume was quickly dispersed, with CH_4 enhancement barely exceeding 100 ppb beyond 300 m downwind the release point (Figure 10). Such active eddies and their efficient transport of CH_4 plume persisted into the afternoon.
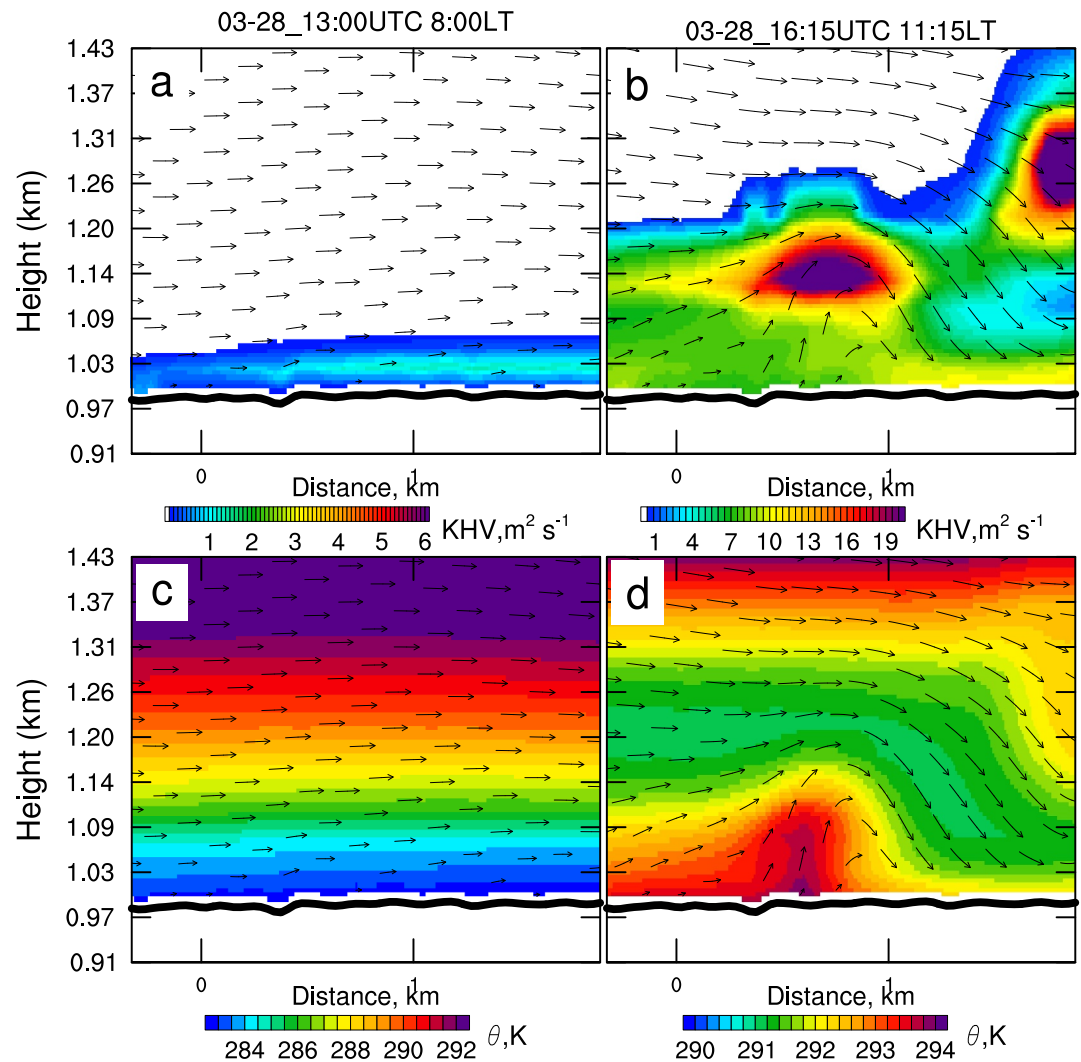
Figure 8. Vertical cross-section of (a), (b) vertical mixing coefficient (KHV) and (c), (d) potential temperature (θ) during (left) sunrise and (right) noon time.

The ratios of simulated to observed cross-plume enhancements can be used to calibrate the greenhouse gas emission rates (Ye et al., 2020). Thus, observed and simulated CH_4 along the short route at 250 m from the release during two morning release windows are examined in Figures 12–14. The simulated CH_4 enhancements at 5-min resolution were more gradual than observations, regardless of which SGS turbulence closure is chosen. The range of simulated CH_4 enhancement (0.8–1.8 ppm) was narrower than the observed range (~0.4–2.6 ppm) during sunrise (Figure 12). The WRF-GHG LES underestimates the enhancement range due to insufficient grid resolution to resolve fine-scale processes and the averaging effect of mixing parameterization. During stable conditions at this time, ubiquitous turbulent eddies have not yet developed, and the near-surface stable boundary layer was characterized by intermittent turbulent events and submeso motions (Banta et al., 2007; Cava et al., 2019). The WRF-GHG LES model simulates mixing processes through the subgrid mixing parameterization solely and therefore cannot fully resolve these processes. The subgrid mixing parameterization tries to simulate the mean effects of unresolved motions/mixing in the form of an ensemble average (Mellor & Yamada, 1974; Nakanishi & Niino, 2004; Sun & Chang, 1986; Wyngaard & Coté, 1974). This averaging effect causes WRF-GHG LES to underestimate the variation of CH_4 plume impacted by the intermittent smaller-scale motions/mixing. Given the instantaneous and averaging characteristics of observed and simulated CH_4 plumes respectively, certain averaging processes for the observed plumes are necessary before using the ratio of simulated and observed cross-plume enhancement to calibrate/scale CH_4 emission rates.
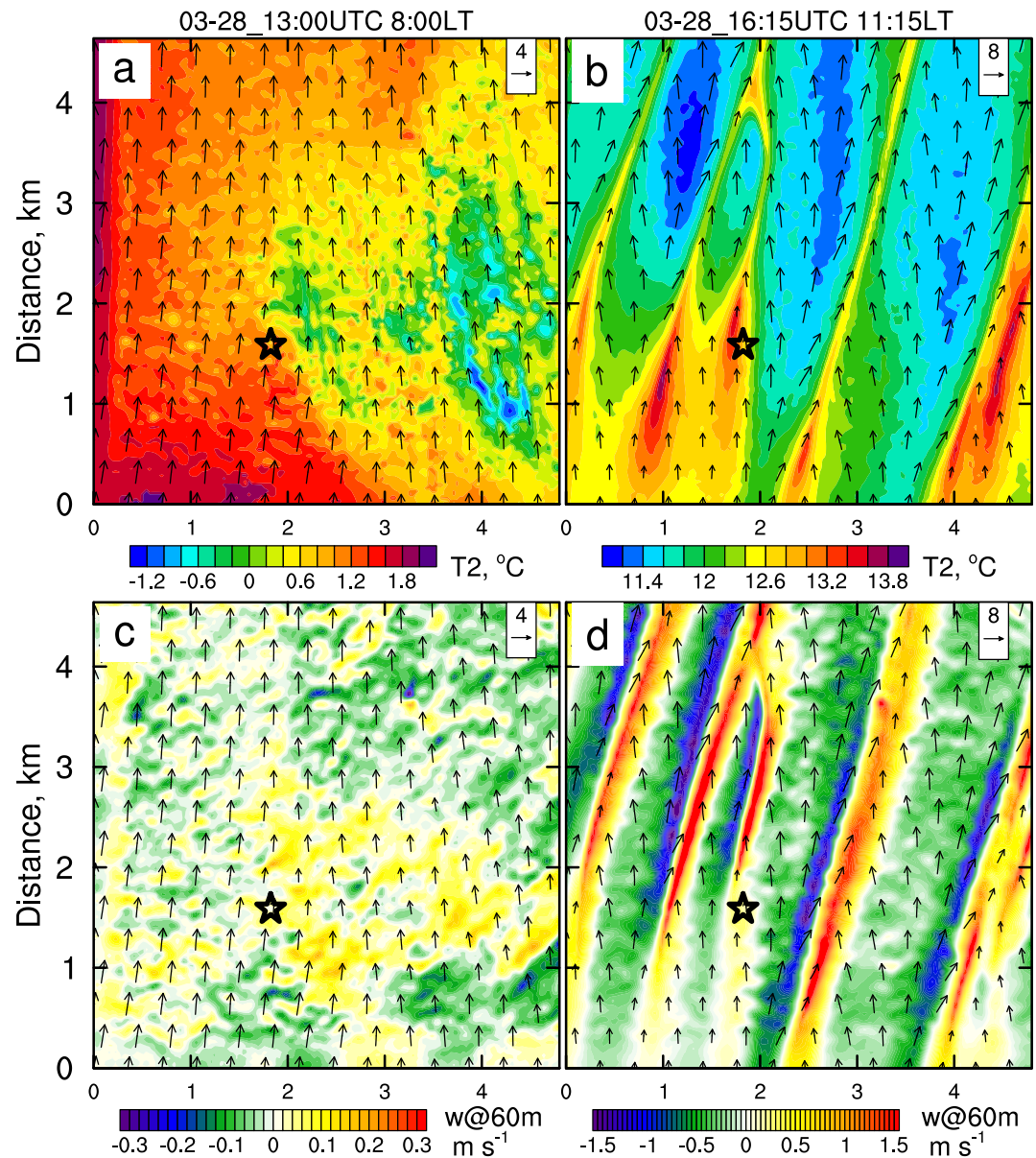
Figure 9. Horizontal spatial distribution of (a), (b) surface temperature at 2 m above the ground (T2) and (c), (d) vertical wind speed at 60 m AGL overlaid with horizontal wind vectors during (left) sunrise and (right) noon time. The release site is marked using a star.

The simulated CH_4 plume enhancement is significantly impacted by the grid resolution and different SGS turbulence closures. The simulated cross-plume CH_4 enhancements in domain 3 (160 m grid spacing) and domain 4 (32 m grid spacing) are compared in Figure 12. With a grid spacing of 160 m, the CH_4 enhancement is greatly reduced in domain 3 compared to domain 4. As a result, domain 3 is not able to capture CH_4 enhancements above 0.5 ppm at sunrise time. We further compared three different SGS turbulence closures. The Smagorinsky closure (KM3) simulates stronger vertical mixing coefficient during the early morning at 7:35–8:05 a.m., which reduces the near surface potential temperature inversion compared with that simulated by the other two SGS closures (Figure 13). As a result, the Smagorinsky closure (KM3) simulates more plume dispersion and weaker CH_4 enhancement compared to the other two (Figures 12a–12c). During the same period, the TKE-1.5 closure (KM2) and the 3D-TKE scheme (KM5) simulated CH_4 plumes with substantial variations, while Smagorinsky (KM3) simulated a roughly constant plume (Figure 12) again due to excessive mixing (Figure 13). In comparison, during
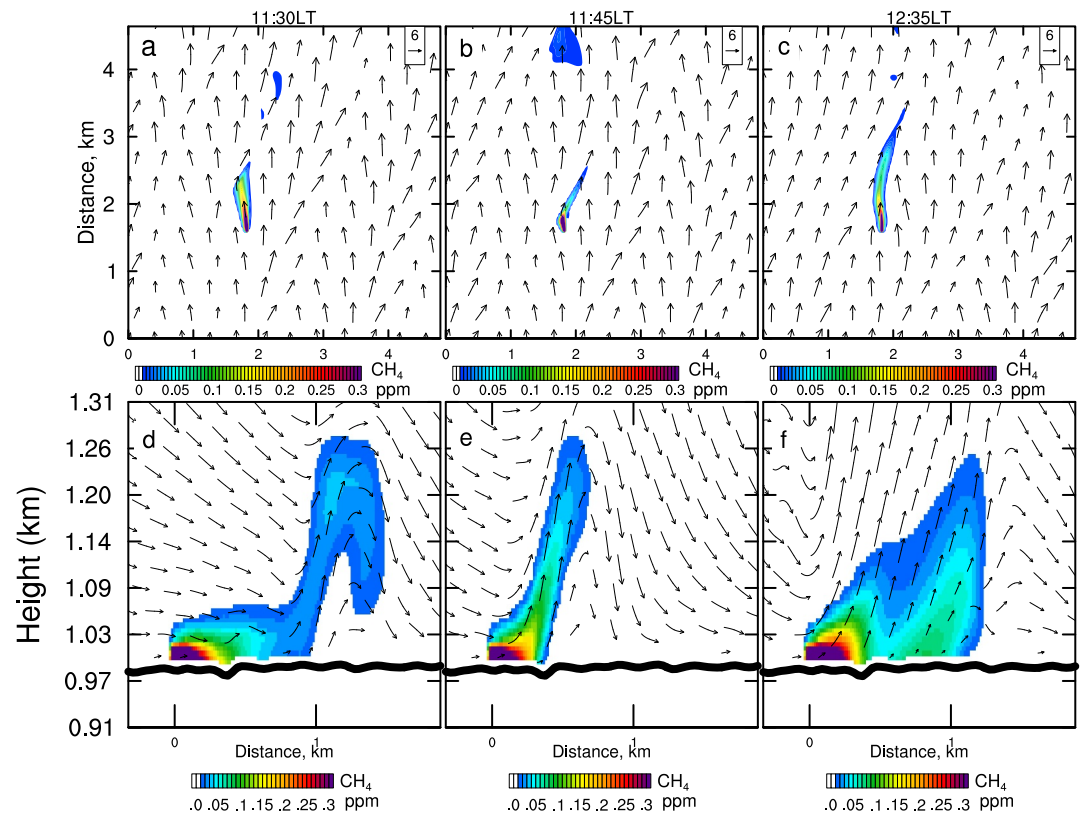
Figure 10. (a), (b), (c) Horizontal spatial distribution and (d), (e), (f) vertical cross-section of CH$_4$ enhancement plumes overlaid with wind vectors at (left to right) 11:30, 11:45, and 12:35 local time.

8:35–9:30 a.m., all three closures overestimated the CH$_4$ enhancement by up to 300 ppb (Figure 14) and the difference between mixing coefficients from the three SGS closures becomes less prominent (Figure not shown).

The measurement team also noticed consistent minor spikes in CH$_4$ concentration originating roughly above a marked high-pressure pipeline along the long route, which appears as a slight enhancement region on the northernmost leg of the long route in Figure 3 near 100°59'30"W. Such a leak would normally be below the actionable threshold for operators, since the excursion was less than 10 ppb above the roughly 2.2 ppm site background. Few sensors would have the quantification precision necessary to even notice it. It is worth noting that the field site, like other sites in the oil and gas extraction regions, may be subject to similar minor leaks.

While the LI-COR sensor was measuring CH$_4$ on the routes, the OGI camera was deployed on a UAS to visualize CH$_4$ plume at ∼10 m above the release site. However, during sunrise on March 28, it was cold (∼1°C). With the sun still too low to sufficiently warm the ground, pipe, and surrounding structures, the temperatures across the entire area were nearly uniform. As a result, the camera could not confidently distinguish the plume, and the quantitative OGI interface was not able to analyze the gas concentration. No video was recorded by the OGI camera later in the day due to high winds (>8 m s^{-1}, Figure 6d), which might cause instability or even damage to the camera. Thus, these conditions represent the limitations of using the OGI camera to detect CH$_4$ plumes. On the afternoon of the previous day (27 Mar. 2024) with weaker winds, the OGI camera was able to identify the CH$_4$ plume within 20–30 m of a release at a similar rate (∼17 kg hr^{-1}).

The investigation of CH$_4$ plumes in Pampa demonstrated that combining mobile LI-COR 7810 measurements with high-resolution WRF-GHG LES can be used to understand CH$_4$ plume behavior under variable atmospheric conditions, providing guidance for quantifying CH$_4$ emissions from point sources. To further demonstrate its generalizability, we used a similar approach to examine CH$_4$ plumes during the morning transition on 23 June 2024 at the Muegge cattle farm, located ∼6 km northwest of the SGP ARM site. The WRF-GHG LES simulation used a prior emission rate of 100 kg hr^{-1} at the cattle farm. Based on the ratio of observed to simulated CH$_4$ plumes (a method used in Barkley et al., 2019; Barkley et al., 2017), the farm's emission rate was estimated to be
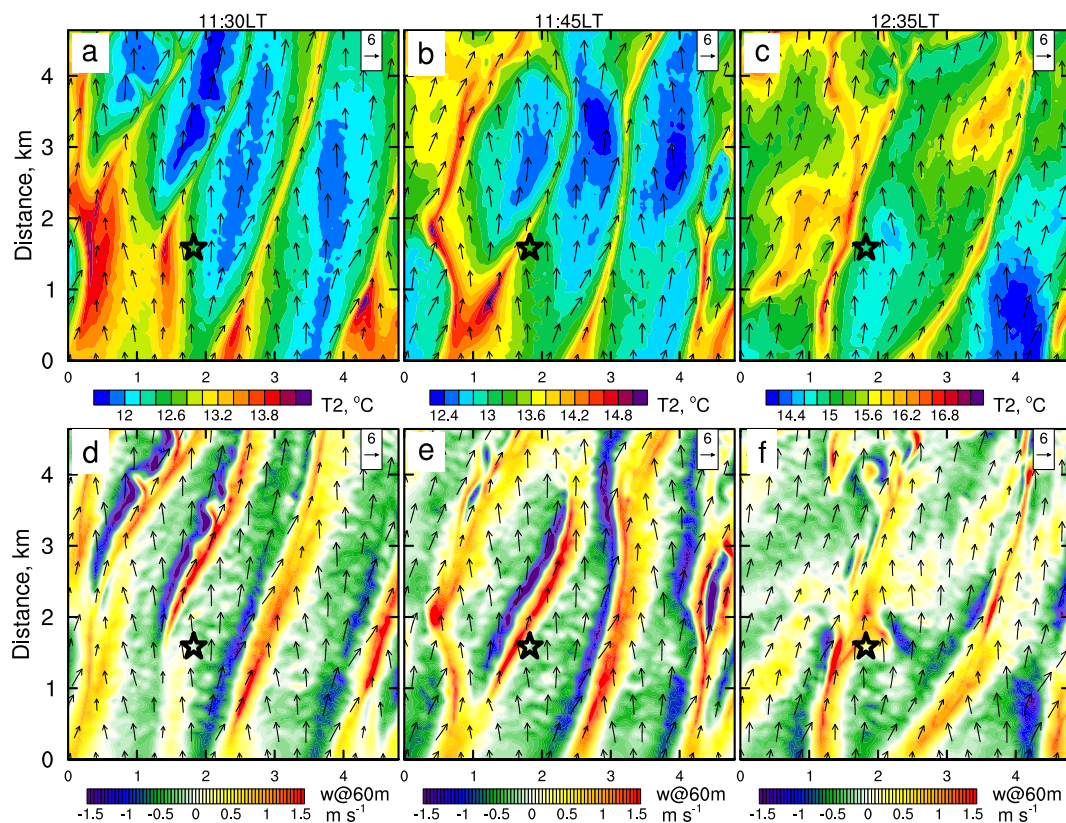
Figure 11. Horizontal spatial distribution of (a), (b), (c) surface temperature at 2 m above the ground (T2) and (d), (e), (f) vertical wind speed overlaid with horizontal wind vectors at (left to right) 11:30, 11:45, and 12:35 local time.
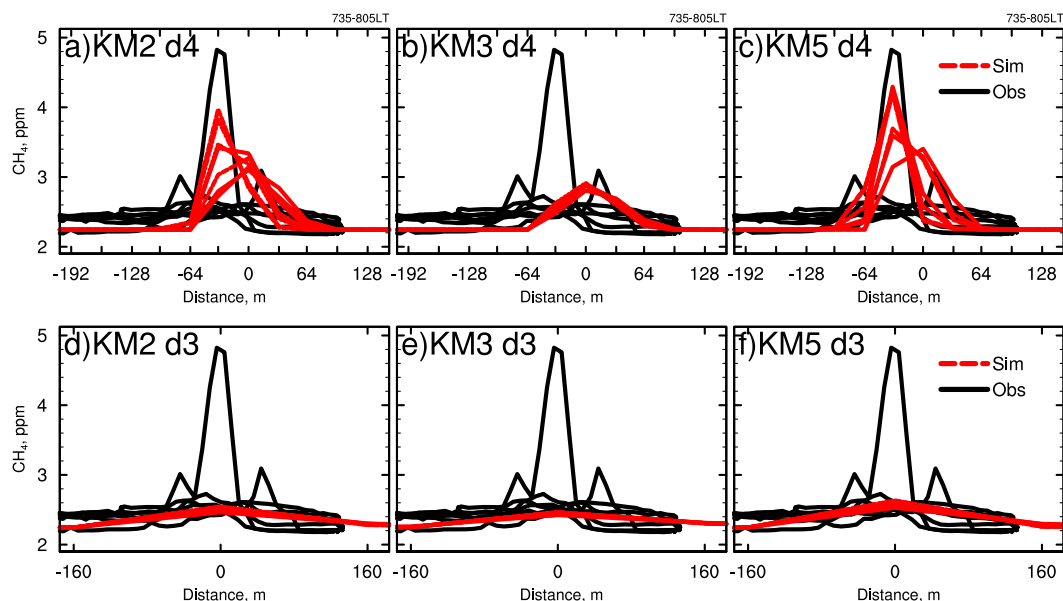

Figure 12. CH$_4$ mixing ratios in the west-to-east direction along the short route (250 m north of the release site) observed and simulated (a), (b), (c) using three subgrid-scale (SGS) mixing closures, that is, KM2 (1.5 order TKE closure), KM3 (first-order Smagorinsky closure), KM5 (scale-aware 3D-TKE scheme) in domain 4 and (d), (e), (f) domain 3 during 7:35–8:05 a. m. Multiple trips were made during observation. Each black line represents observation during one trip.
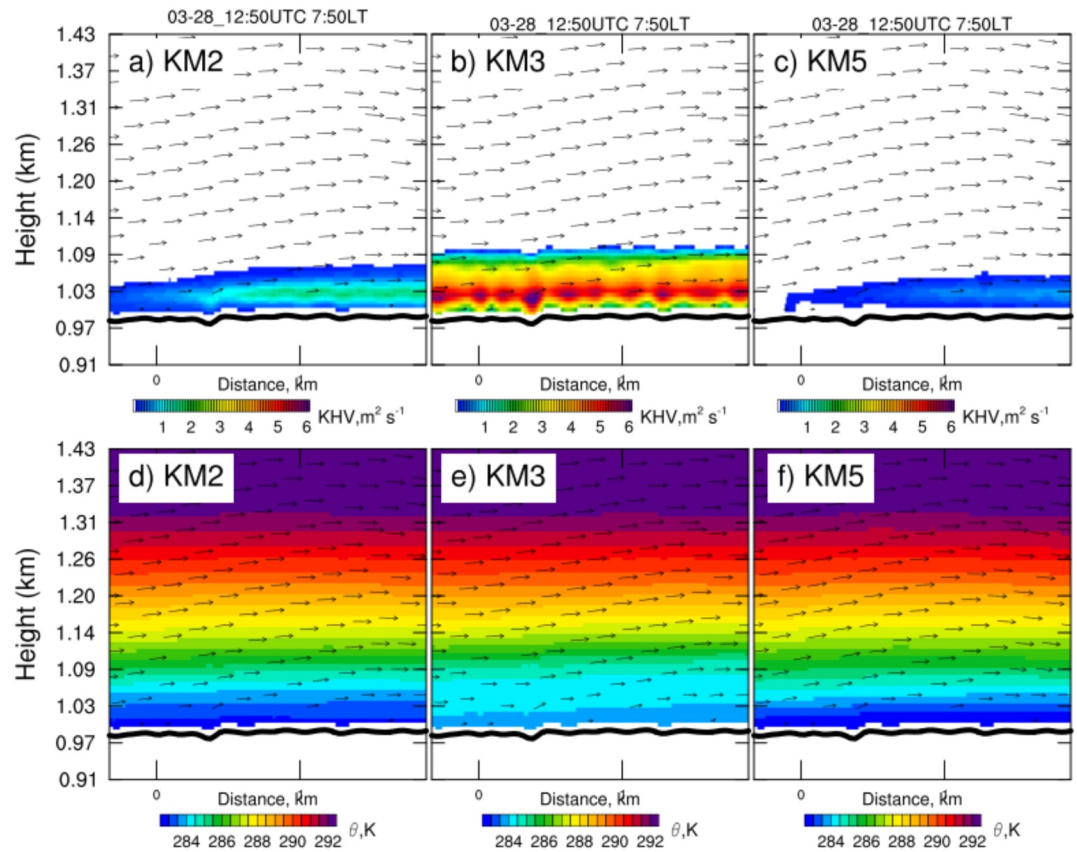
Figure 13. Vertical cross-section of simulated (a), (b), (c) vertical mixing coefficient (KHV) and (d), (e), (f) potential temperature (θ) using three subgrid-scale (SGS) mixing closures, that is, KM2 (1.5 order TKE closure), KM3 (first-order Smagorinsky closure), KM5 (scale-aware 3D-TKE scheme).

$\sim$65 kg hr^{-1} at 6:00 a.m. Similar to the Pampa experiment, the boundary layer transition during the early morning exerted significant impact on CH$_4$ plumes (Figure 15). At 6:00 a.m., the CH$_4$ plume extended a few kilometers downstream within the stable boundary layer, which explains the nighttime CH$_4$ peaks often observed at the ARM site in the presence of northwesterly winds (Wang et al., 2024). At 9:00 a.m., the convective boundary layer already growed, as indicated by the staggered wind vectors induced by large eddies, which led to a shorter surface CH$_4$ plume. At this time, the plume enhancement decreased to tens of ppb beyond 1 km with an emission rate of 100 kg hr^{-1}. The growth of the convective boundary layer occurred earlier ($\sim$9:00 a.m.) on this summer day at the Muegge Farm compared to the Pampa case on 28 March 2024 ($\sim$11:00 a.m.). Further details on the characteristics
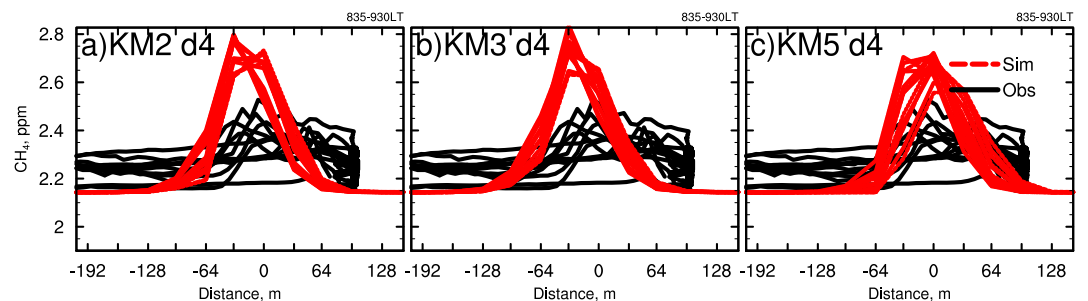

Figure 14. CH$_4$ mixing ratios along the short route observed and simulated (a), (b), (c) using three subgrid-scale (SGS) mixing closures, that is, KM2 (1.5 order TKE closure), KM3 (first-order Smagorinsky closure), KM5 (scale-aware 3D-TKE scheme) in domain 4 during 8:35–9:30 a.m.
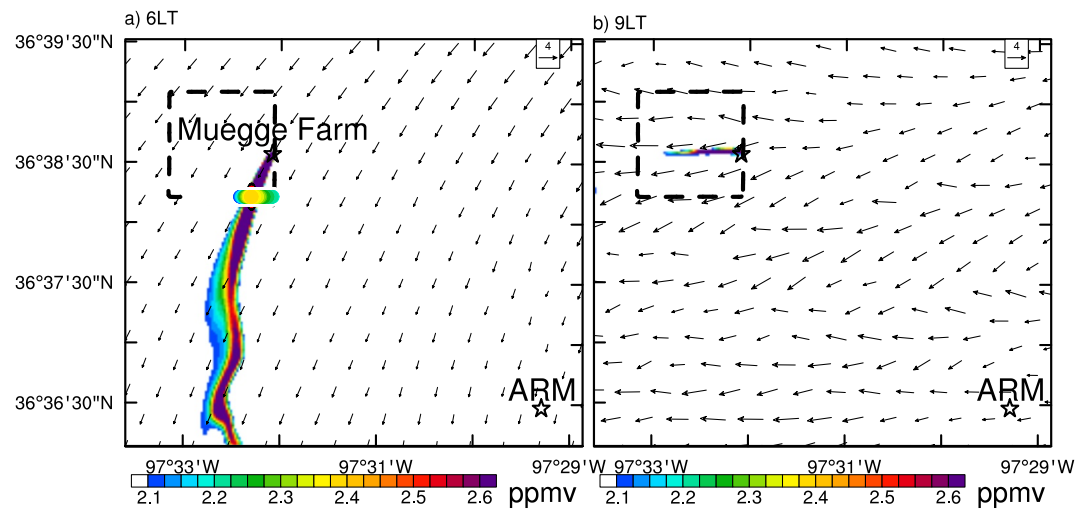
Figure 15. CH_4 plume at (a) 6:00 a.m. and (b) 9:00 a.m. on 23 June 2024 simulated with WRF-GHG LES with an emission rate of 100 kg hr^{-1}. The observed CH_4 concentration at 6:00 a.m. is overlaid in panel (a). The dashed box (1.6× 1.6 km) marks the public road where mobile LICOR-7810 observations were taken around 6:00 a.m., while there was no observation at 9:00 a.m.

of CH_4 at this ARM site and the impact of the Muegge Farm are beyond the scope of this work and will be addressed in a separate study.

4. Conclusions and Discussion

A controlled CH_4 release experiment was conducted on 28 March 2024 in Pampa, Texas. While an OGI camera was mounted on a UAS to monitor the CH_4 plume directly above the release point, a LI-COR 7810 was deployed on a mobile van to measure downstream plumes along the routes ~250 m to 1.5 km from the release point. Substantial changes in CH_4 plumes were observed throughout the sunrise time. At a release rate of 17.5 kg hr^{-1}, the maximum CH_4 enhancement measured by LI-COR 7810 was 2.6 ppm at sunrise (7:36 a.m.), 250 m from the release location. Within half an hour after sunrise, the enhancement dropped to 0.3–0.4 ppm. The enhancement further decreased to 0.2 ppm by 10 a.m. and was less than 0.1 ppm after 11:30 a.m. After 1 p.m., the plume enhancement was lower than 60 ppb. At 1.5 km from the release location, a notable CH_4 enhancement of ~100 ppb was observed only at sunrise. Due to the low temperature (1°C) at sunrise and insufficient thermal contrast, the OGI camera failed to detect the CH_4 plume. Later in the morning, the OGI camera could not operate due to strong winds (>8 m s^{-1}). This suggests that the detection and quantification of CH_4 emissions a few hundred meters from a super emitter (>10 kg hr^{-1}) are possible with appropriate tools (e.g., LI-COR 7810), while the application of OGI camera is limited by weather conditions.

The WRF-GHG LES with 32 m grid spacing successfully reproduced the observed CH_4 enhancements in both location and magnitude, with reasonable uncertainties attributed to SGS turbulence treatments. The simulated meteorology was examined in terms of the boundary layer variation and its impact on CH_4 plumes. At sunrise, the near surface air was very stable and the CH_4 plume was barely vertically dispersed. Thus, the CH_4 plume was confined within a very shallow surface layer and lengthily stretched downwind. The model underestimated the CH_4 enhancement at sunrise, likely due to the ensemble average characteristic of the mixing parameterization, which smooths out the intermittent turbulence and its impact on CH_4 plume. After 11 a.m., active large eddies in the convective boundary layer effectively dilute the CH_4 plume. Thus, the CH_4 enhancement rarely exceeded 100 ppb beyond 300 m from the release point. The simulated CH_4 plume enhancement is significantly impacted by the grid resolution and different SGS turbulence closures. A grid spacing of 160 m is apparently inadequate for resolving the narrow CH_4 plumes released from essentially a point source.

This study demonstrates the capability of WRF-GHG LES in simulating CH_4 over real terrain with varying atmospheric stability, offering valuable insights into the behavior and detection of CH_4 plumes. However, the intensive computational demands of LES limit its applications to mainly small domains and short time periods,

posing challenges for accurate CH_4 quantification over large areas and long periods. Additionally, although our simulations at the Pampa site and the SGP ARM site nearly cover the full cycle of the diurnal variation in the atmospheric boundary layer, the performance of this approach during the early evening boundary layer transition remains untested. Further investigation during this critical transition period is needed, as it involves complex processes that are prominent scientific questions in their own right (Acevedo & Fitzjarrald, 2001; Bonin et al., 2013). Building-resolving LES can also provide a more accurate representation of how infrastructure affects emission and dispersion patterns for oil and gas fields (Li et al., 2024).

Despite these limitations, high-resolution LES simulations are crucial for resolving CH_4 plumes as narrow as 60–90 m and provide practical guidance for emission detection and quantification, for example, the necessary accuracy and detection range needed. Within the convective boundary layer, instruments with an accuracy of at least tens of ppb need to be deployed within a few hundred meters to detect CH_4 plumes with moderate emission rates of tens of kg hr^{-1}. Given the instantaneous and averaging characteristics of observed and simulated CH_4 plumes, respectively, appropriate averaging processes for the observed plumes are necessary before using the ratio of simulated to observed cross-plume enhancements to calibrate/scale CH_4 emission rates during the early morning.

Data Availability Statement

The operational Global Forecast System (GFS) 0.25-degree-resolution data (National Centers for Environmental Prediction/National Weather Service/NOAA/U.S. Department of Commerce, 2015) was downloaded from https://noaa-gfs-bdp-pds.s3.amazonaws.com/index.html. Copernicus Atmosphere Monitoring Service (CAMS) CH_4 global simulation outputs (Agustí-Panareda et al., 2023) were downloaded from https://ads.atmosphere.copernicus.eu/datasets/cams-global-greenhouse-gas-inversion?tab=download. The Meteorological Assimilation Data Ingest System (MADIS) data (NOAA, 2025) were downloaded from https://madis.ncep.noaa.gov/madis_datasets.shtml. Data and scripts produced from this study have been archived at CAPS website (https://caps.ou.edu/micronet/WRF_GHG_Forecasting_Pampa.html) and the Luster NSF projects data server at the San Diego Supercomputer Center (/expanse/luster/projects/uok114/xhu2).

References

Acevedo, O. C., & Fitzjarrald, D. R. (2001). The early evening surface-layer transition: Temporal and spatial variability. *Journal of the Atmospheric Sciences*, *58*(17), 2650–2667. https://doi.org/10.1175/1520-0469(2001)058<2650:TEESLT>2.0.CO;2

Agustí-Panareda, A., Barré, J., Massart, S., Inness, A., Aben, I., Ades, M., et al. (2023). Technical note: The CAMS greenhouse gas reanalysis from 2003 to 2020. *Atmospheric Chemistry and Physics*, *23*(6), 3829–3859. [Dataset]. https://doi.org/10.5194/acp-23-3829-2023

Ahmadov, R., Gerbig, C., Kretschmer, R., Koerner, S., Neininger, B., Dolman, A. J., & Sarrat, C. (2007). Mesoscale covariance of transport and CO_2 fluxes: Evidence from observations and simulations using the WRF-VPRM coupled atmosphere-biosphere model. *Journal of Geophysical Research*, *112*(D22), D22107. https://doi.org/10.1029/2007jd008552

Arya, S. P. (1999). *Air pollution meteorology and dispersion*. Oxford University Press.

Ballav, S., Patra, P. K., Sawa, Y., Matsueda, H., Adachi, A., Onogi, S., et al. (2016). Simulation of CO_2 concentrations at Tsukuba tall tower using WRF-CO_2 tracer transport model. *Journal of Earth System Science*, *125*(1), 47–64. https://doi.org/10.1007/s12040-015-0653-y

Banta, R. M., Mahrt, L., Vickers, D., Sun, J., Balsley, B. B., Pichugina, Y. L., & Williams, E. J. (2007). The very stable boundary layer on nights with weak low-level jets. *Journal of the Atmospheric Sciences*, *64*(9), 3068–3090. https://doi.org/10.1175/JAS4002.1

Barkley, Z., Davis, K., Miles, N., Richardson, S., Deng, A., Hmiel, B., et al. (2023). Quantification of oil and gas methane emissions in the Delaware and Marcellus basins using a network of continuous tower-based measurements. *Atmospheric Chemistry and Physics*, *23*(11), 6127–6144. https://doi.org/10.5194/acp-23-6127-2023

Barkley, Z. R., Lauvaux, T., Davis, K. J., Deng, A., Fried, A., Weibring, P., et al. (2019). Estimating methane emissions from underground coal and natural gas production in southwestern Pennsylvania. *Geophysical Research Letters*, *46*(8), 4531–4540. https://doi.org/10.1029/2019GL082131

Barkley, Z. R., Lauvaux, T., Davis, K. J., Deng, A., Miles, N. L., Richardson, S. J., et al. (2017). Quantifying methane emissions from natural gas production in north-eastern Pennsylvania. *Atmospheric Chemistry and Physics*, *17*(22), 13941–13966. https://doi.org/10.5194/acp-17-13941-2017

Beare, R. J. (2008). The role of shear in the morning transition boundary layer. *Boundary-Layer Meteorology*, *129*(3), 395–410. https://doi.org/10.1007/s10546-008-9324-8

Bell, C., Ilonze, C., Duggan, A., & Zimmerle, D. (2023). Performance of continuous emission monitoring solutions under a single-blind controlled testing protocol. *Environmental Science and Technology*, *57*(14), 5794–5805. https://doi.org/10.1021/acs.est.2c09235

Bergau, M., Strahl, T., Ludlum, K., Scherer, B., & Wöllenstein, J. (2024). Flow rate quantification of small methane leaks using laser spectroscopy and deep learning. *Process Safety and Environmental Protection*, *182*, 752–759. https://doi.org/10.1016/j.psep.2023.11.059

Bloom, A. A., Bowman, K. W., Lee, M., Turner, A. J., Schroeder, R., Worden, J. R., & Jacob, D. J. (2017). *CMS: Global 0.5-deg wetland methane emissions and uncertainty (WetCHARTs v1.0)*. ORNL Distributed Active Archive Center. https://doi.org/10.3334/ORNLDAAC/1502

Bluestein, H. B. (1992). *Synoptic-dynamic meteorology in midlatitudes: Observations and theory of weather systems*. Oxford University Press.

Bonin, T., Chilson, P., Zielke, B., & Fedorovich, E. (2013). Observations of the early evening boundary-layer transition using a small unmanned aerial system. *Boundary-Layer Meteorology*, *146*(1), 119–132. https://doi.org/10.1007/s10546-012-9760-3

Bonin, T. A., Klein, P. M., & Chilson, P. B. (2020). Contrasting characteristics and evolution of southerly low-level jets during different boundary-layer regimes. *Boundary-Layer Meteorology*, *174*(2), 179–202. https://doi.org/10.1007/s10546-019-00481-0

Caulton, D. R., Li, Q., Bou-Zeid, E., Fitts, J. P., Golston, L. M., Pan, D., et al. (2018). Quantifying uncertainties from mobile-laboratory-derived emissions of well pads using inverse Gaussian methods. *Atmospheric Chemistry and Physics*, *18*(20), 15145–15168. https://doi.org/10.5194/acp-18-15145-2018

Cava, D., Mortarini, L., Giostra, U., Acevedo, O., & Katul, G. (2019). Submeso motions and intermittent turbulence across a nocturnal low-level jet: A self-organized criticality analogy. *Boundary-Layer Meteorology*, *172*(1), 17–43. https://doi.org/10.1007/s10546-019-00441-8

Chen, F., & Dudhia, J. (2001). Coupling an advanced land surface-hydrology model with the Penn State-NCAR MM5 modeling system. Part I: Model implementation and sensitivity. *Monthly Weather Review*, *129*(4), 569–585. https://doi.org/10.1175/1520-0493(2001)129<0569:Caalsh>2.0.Co;2

Chen, H. W., Zhang, F., Lauvaux, T., Davis, K. J., Feng, S., Butler, M. P., & Alley, R. B. (2019). Characterization of regional-scale CO_2 transport uncertainties in an ensemble with flow-dependent transport errors. *Geophysical Research Letters*, *46*(7), 4049–4058. https://doi.org/10.1029/2018GL081341

Chen, Y., Sherwin, E. D., Berman, E. S. F., Jones, B. B., Gordon, M. P., Wetherley, E. B., et al. (2022). Quantifying regional methane emissions in the New Mexico permian basin with a comprehensive aerial survey. *Environmental Science and Technology*, *56*(7), 4317–4323. https://doi.org/10.1021/acs.est.1c06458

Chen, Z., El Abbadi, S. H., Sherwin, E. D., Burdeau, P. M., Rutherford, J. S., Chen, Y., et al. (2024). Comparing continuous methane monitoring technologies for high-volume emissions: A single-blind controlled release study. *ACS ES&T Air*, *1*(8), 871–884. https://doi.org/10.1021/acsestair.4c00015

Chu, X., Xue, L., Geerts, B., Rasmussen, R., & Breed, D. (2014). A case study of radar observations and WRF LES simulations of the impact of ground-based glaciogenic seeding on orographic clouds and precipitation. Part I: Observations and model validations. *Journal of Applied Meteorology and Climatology*, *53*(10), 2264–2286. https://doi.org/10.1175/JAMC-D-14-0017.1

Ciais, P., Rayner, P., Chevallier, F., Bousquet, P., Logan, M., Peylin, P., & Ramonet, M. (2010). Atmospheric inversions for estimating CO2 fluxes: Methods and perspectives. *Climatic Change*, *103*(1), 69–92. https://doi.org/10.1007/s10584-010-9909-3

Delkash, M., Zhou, B., Han, B., Chow, F. K., Rella, C. W., & Imhoff, P. T. (2016). Short-term landfill methane emissions dependency on wind. *Waste Management*, *55*, 288–298. https://doi.org/10.1016/j.wasman.2016.02.009

Diaz-Isaac, L. I., Lauvaux, T., & Davis, K. J. (2018). Impact of physical parameterizations and initial conditions on simulated atmospheric transport and CO_2 mole fractions in the US Midwest. *Atmospheric Chemistry and Physics*, *18*(20), 14813–14835. https://doi.org/10.5194/acp-18-14813-2018

Dong, X. Y., Yue, M., Jiang, Y. J., Hu, X.-M., Ma, Q. L., Pu, J. J., & Zhou, G. Q. (2021). Analysis of CO_2 spatio-temporal variations in China using a weather-biosphere online coupled model. *Atmospheric Chemistry and Physics*, *21*(9), 7217–7233. https://doi.org/10.5194/acp-21-7217-2021

Dudhia, J. (1989). Numerical study of convection observed during the winter monsoon experiment using a mesoscale two-dimensional model. *Journal of the Atmospheric Sciences*, *46*(20), 3077–3107. https://doi.org/10.1175/1520-0469(1989)046<3077:Nsocod>2.0.Co;2

Feng, S., Lauvaux, T., Davis, K. J., Keller, K., Zhou, Y., Williams, C., et al. (2019). Seasonal characteristics of model uncertainties from biogenic fluxes, transport, and large-scale boundary inflow in atmospheric CO_2 simulations over north America. *Journal of Geophysical Research: Atmospheres*, *124*(24), 14325–14346. https://doi.org/10.1029/2019JD031165

Feng, S., Lauvaux, T., Keller, K., Davis, K. J., Rayner, P., Oda, T., & Gurney, K. R. (2019). A road map for improving the treatment of uncertainties in high-resolution regional carbon flux inverse estimates. *Geophysical Research Letters*, *46*(22), 13461–13469. https://doi.org/10.1029/2019GL082987

Flesch, T. K., Wilson, J. D., Harper, L. A., Crenna, B. P., & Sharpe, R. R. (2004). Deducing ground-to-air emissions from observed trace gas concentrations: A field trial. *Journal of Applied Meteorology*, *43*(3), 487–502. https://doi.org/10.1175/1520-0450(2004)043<0487:DGEFOT>2.0.CO;2

Francoeur, C. B., McDonald, B. C., Gilman, J. B., Zarzana, K. J., Dix, B., Brown, S. S., et al. (2021). Quantifying methane and ozone precursor emissions from oil and gas production regions across the contiguous US. *Environmental Science and Technology*, *55*(13), 9129–9139. https://doi.org/10.1021/acs.est.0c07352

Gibbs, J. A., & Fedorovich, E. (2014). Comparison of convective boundary layer velocity spectra retrieved from large-eddy-simulation and weather research and forecasting model data. *Journal of Applied Meteorology and Climatology*, *53*(2), 377–394. https://doi.org/10.1175/JAMC-D-13-033.1

Gorchov Negron, A. M., McDonald, B. C., McKeen, S. A., Peischl, J., Ahmadov, R., de Gouw, J. A., et al. (2018). Development of a fuel-based oil and gas inventory of nitrogen oxides emissions. *Environmental Science and Technology*, *52*(17), 10175–10185. https://doi.org/10.1021/acs.est.8b02245

Honeycutt, W. T., Kim, T., Ley, M. T., & Materer, N. F. (2021). Sensor array for wireless remote monitoring of carbon dioxide and methane near carbon sequestration and oil recovery sites. *RSC Advances*, *11*(12), 6972–6984. https://doi.org/10.1039/D0RA08593F

Honeycutt, W. T., Ley, M. T., & Materer, N. F. (2019). Precision and limits of detection for selected commercially available, low-cost carbon dioxide and methane gas sensors. *Sensors*, *19*(14), 3157. https://doi.org/10.3390/s19143157

Hong, S.-Y. (2010). A new stable boundary-layer mixing scheme and its impact on the simulated East Asian summer monsoon. *Quarterly Journal of the Royal Meteorological Society*, *136*(651), 1481–1496. https://doi.org/10.1002/qj.665

Hu, X.-M., Crowell, S., Wang, Q., Zhang, Y., Davis, K. J., Xue, M., et al. (2020). Dynamical Downscaling of CO_2 in 2016 over the contiguous United States using WRF-VPRM, a weather-biosphere-online-coupled model. *Journal of Advances in Modeling Earth Systems*, *12*(4), e2019MS001875. https://doi.org/10.1029/2019ms001875

Hu, X.-M., Doughty, D. C., Sanchez, K. J., Joseph, E., & Fuentes, J. D. (2012). Ozone variability in the atmospheric boundary layer in Maryland and its implications for vertical transport model. *Atmospheric Environment*, *46*, 354–364. https://doi.org/10.1016/j.atmosenv.2011.09.054

Hu, X.-M., Gourdji, S. M., Davis, K. J., Wang, Q., Zhang, Y., Xue, M., et al. (2021). Implementation of improved parameterization of terrestrial flux in WRF-VPRM improves the simulation of nighttime CO_2 peaks and a daytime CO_2 band ahead of a cold front. *Journal of Geophysical Research: Atmospheres*, *126*(10), e2020JD034362. https://doi.org/10.1029/2020JD034362

Hu, X.-M., Hu, J., Gao, L., Cai, C., Jiang, Y., Xue, M., et al. (2021). Multisensor and multimodel monitoring and investigation of a wintertime air pollution event ahead of a cold front over eastern China. *Journal of Geophysical Research: Atmospheres*, *126*(10). https://doi.org/10.1029/2020jd033538

Hu, X.-M., Klein, P. M., & Xue, M. (2013). Evaluation of the updated YSU planetary boundary layer scheme within WRF for wind resource and air quality assessments. *Journal of Geophysical Research-Atmospheres*, *118*(18), 10490–10505. https://doi.org/10.1002/jgrd.50823

Hu, X.-M., Li, X., Zhou, B., & Xue, M. (2024). *Air pollution meteorology* reference Module in earth Systems and environmental sciences. Elsevier.

Hu, X.-M., Nielsen-Gammon, J. W., & Zhang, F. (2010). Evaluation of three planetary boundary layer schemes in the WRF model. *Journal of Applied Meteorology and Climatology*, *49*(9), 1831–1844. https://doi.org/10.1175/2010jamc2432.1

Hu, X.-M., Park, J., Supinie, T., Snook, N. A., Xue, M., Brewster, K. A., et al. (2023). Diagnosing near-surface model errors with candidate physics parameterization schemes for the multiphysics rapid refresh forecast system (RRFS) ensemble during winter over the northeastern United States and southern Great Plains. *Monthly Weather Review*, *151*(1), 39–61. https://doi.org/10.1175/MWR-D-22-0085.1

Hu, X.-M., Xue, M., Gao, L., & Crowell, S. (2021). Impact of 2019 mid-west flood on CO2 and CH4 using yearly WRF-GHG simulations over the contiguous United States. In *Paper presented at the AGU fall meeting abstracts*. https://doi.org/10.1002/essoar.10508159.1

Hu, X.-M., Xue, M., Kong, F. Y., & Zhang, H. L. (2019). Meteorological conditions during an ozone episode in dallas-fort worth, Texas, and impact of their modeling uncertainties on air quality prediction. *Journal of Geophysical Research-Atmospheres*, *124*(4), 1941–1961. https://doi.org/10.1029/2018jd029791

Hu, X.-M., Xue, M., & Li, X. (2019). The use of high-resolution sounding data to evaluate and optimize nonlocal PBL schemes for simulating the slightly stable upper convective boundary layer. *Monthly Weather Review*, *147*(10), 3825–3841. https://doi.org/10.1175/mwr-d-19-0085.1

ICF International. (2014). Economic analysis of methane emission reduction opportunities in the U.S. Onshore oil and natural gas industries. Retrieved from https://www.edf.org/sites/default/files/methane_cost_curve_report.pdf

IPCC. (2021). *Climate change 2021: The physical science basis. Contribution of working group I to the sixth assessment report of the intergovernmental panel on climate change*. Cambridge University Press. https://doi.org/10.1017/9781009157896

Kumar, P., Caldow, C., Broquet, G., Shah, A., Laurent, O., Yver-Kwok, C., et al. (2024). Detection and long-term quantification of methane emissions from an active landfill. *Atmospheric Measurement Techniques*, *17*(4), 1229–1250. https://doi.org/10.5194/amt-17-1229-2024

Lapworth, A. (2006). The morning transition of the nocturnal boundary layer. *Boundary-Layer Meteorology*, *119*(3), 501–526. https://doi.org/10.1007/s10546-005-9046-0

Lauvaux, T., Giron, C., Mazzolini, M., d'Aspremont, A., Duren, R., Cusworth, D., et al. (2022). Global assessment of oil and gas methane ultra-emitters. *Science*, *375*(6580), 557–561. https://doi.org/10.1126/science.abj4351

Li, Q., Padilla, L., Thompson, T., Xiao, S., Mohr, E. J., Zhou, X., et al. (2024). A modeling framework to assess fenceline monitoring and self-reported upset emissions of benzene from multiple oil refineries in Texas. *Atmospheric Environment X*, *23*, 100281. https://doi.org/10.1016/j.aeaoa.2024.100281

Li, X., Hu, X.-M., Cai, C., Jia, Q., Zhang, Y., Liu, J., et al. (2020). Terrestrial CO2 fluxes, concentrations, sources and budget in northeast China: Observational and modeling studies. *Journal of Geophysical Research: Atmospheres*, *125*(6), e2019JD031686. https://doi.org/10.1029/2019jd031686

Li, X., Quan, W., Hu, X.-M., Jia, Q., Ma, Z., Dong, F., et al. (2023). On the large variation in atmospheric CO_2 concentration at Shangdianzi GAW station during two dust storm events in March 2021. *Atmosphere*, *14*(9), 1348. https://doi.org/10.3390/atmos14091348

Liu, C., Huang, J., Fedorovich, E., Hu, X.-M., Wang, Y., & Lee, X. (2018). The effect of aerosol radiative heating on turbulence statistics and spectra in the atmospheric convective boundary layer: A large-eddy simulation study. *Atmosphere*, *9*(9), 347. https://doi.org/10.3390/atmos9090347

Log, T., Pedersen, W. B., & Moumets, H. (2019). Optical gas imaging (OGI) as a moderator for interdisciplinary cooperation, reduced emissions and increased safety. *Energies*, *12*(8), 1454. https://doi.org/10.3390/en12081454

Lyman, S. N., Tran, T., Mansfield, M. L., & Ravikumar, A. P. (2019). Aerial and ground-based optical gas imaging survey of Uinta Basin oil and gas wells. *Elementa-Science of the Anthropocene*, *7*. https://doi.org/10.1525/elementa.381

Mahadevan, P., Wofsy, S. C., Matross, D. M., Xiao, X. M., Dunn, A. L., Lin, J. C., et al. (2008). A satellite-based biosphere parameterization for net ecosystem CO2 exchange: Vegetation Photosynthesis and Respiration Model (VPRM). *Global Biogeochemical Cycles*, *22*(2), Gb2005. https://doi.org/10.1029/2006gb002735

Mellor, G. L., & Yamada, T. (1974). Hierarchy of turbulence closure models for planetary boundary-layers. *Journal of the Atmospheric Sciences*, *31*(7), 1791–1806. https://doi.org/10.1175/1520-0469(1974)031<1791:Ahotcm>2.0.Co;2

Mirocha, J., Kirkil, G., Bou-Zeid, E., Chow, F. K., & Kosović, B. (2013). Transition and equilibration of neutral atmospheric boundary layer flow in one-way nested large-eddy simulations using the weather research and forecasting model. *Monthly Weather Review*, *141*(3), 918–940. https://doi.org/10.1175/MWR-D-11-00263.1

Mirocha, J., Kosović, B., & Kirkil, G. (2014). Resolved turbulence characteristics in large-eddy simulations nested within mesoscale simulations using the weather research and forecasting model. *Monthly Weather Review*, *142*(2), 806–831. https://doi.org/10.1175/MWR-D-13-00064.1

Mlawer, E. J., Taubman, S. J., Brown, P. D., Iacono, M. J., & Clough, S. A. (1997). Radiative transfer for inhomogeneous atmospheres: RRTM, a validated correlated-k model for the longwave. *Journal of Geophysical Research*, *102*(D14), 16663–16682. https://doi.org/10.1029/97jd00237

Nakanishi, M., & Niino, H. (2004). An improved Mellor-Yamada level-3 model with condensation physics: Its design and verification. *Boundary-Layer Meteorology*, *112*(1), 1–31. https://doi.org/10.1023/B:Boun.0000020164.04146.98

National Centers for Environmental Prediction/National Weather Service/NOAA/U.S. Department of Commerce. (2015). *NCEP GFS 0.25 Degree Global Forecast Grids Historical Archive*. [Dataset]. Retrieved from: https://rda.ucar.edu/datasets/dsd084001/

Nieuwstadt, F. T. M. (1992a). A large-eddy simulation of a line source in a convective atmospheric boundary layer—I. Dispersion characteristics. *Atmospheric Environment, Part A: General Topics*, *26*(3), 485–495. https://doi.org/10.1016/0960-1686(92)90331-E

Nieuwstadt, F. T. M. (1992b). A large-eddy simulation of a line source in a convective atmospheric boundary layer—II. Dynamics of a buoyant line source. *Atmospheric Environment, Part A: General Topics*, *26*(3), 497–503. https://doi.org/10.1016/0960-1686(92)90332-F

Nisbet, E. G., Fisher, R. E., Lowry, D., France, J. L., Allen, G., Bakkaloglu, S., et al. (2020). Methane mitigation: Methods to reduce emissions, on the path to the Paris agreement. *Reviews of Geophysics*, *58*(1), e2019RG000675. https://doi.org/10.1029/2019RG000675

NOAA. (2025). Meteorological assimilation data ingest system (MADIS) data. [Dataset] Retrieved from https://madis.ncep.noaa.gov/madis_datasets.shtml

Nutt, K. J., Hempler, N., Maker, G. T., Malcolm, G. P. A., Padgett, M. J., & Gibson, G. M. (2020). Developing a portable gas imaging camera using highly tunable active-illumination and computer vision. *Optics Express*, *28*(13), 18566–18576. https://doi.org/10.1364/oe.389634

Pasquill, F. (1961). The estimation of the dispersion of windborne material. *The Meteorological Magazine*, *90*, 33–49.

Raznjevic, A., van Heerwaarden, C., & Krol, M. (2022). Evaluation of two common source estimation measurement strategies using large-eddy simulation of plume dispersion under neutral atmospheric conditions. *Atmospheric Measurement Techniques*, *15*(11), 3611–3628. https://doi.org/10.5194/amt-15-3611-2022

Riddick, S. N., Ancona, R., Cheptonui, F., Bell, C. S., Duggan, A., Bennett, K. E., & Zimmerle, D. J. (2022). A cautionary report of calculating methane emissions using low-cost fence-line sensors. *Elementa: Science of the Anthropocene*, *10*(1). https://doi.org/10.1525/elementa.2022.00021

Safitri, A., & Mannan, M. S. (2010). Methane gas visualization using infrared imaging system and evaluation of temperature dependence of methane gas emissivity. *Industrial and Engineering Chemistry Research*, *49*(8), 3926–3935. https://doi.org/10.1021/ie901340g

Saunois, M., Martinez, A., Poulter, B., Zhang, Z., Raymond, P., Regnier, P., et al. (2024). Global methane budget 2000-2020. *Earth System Science Data Discussions*, *2024*, 1–147. https://doi.org/10.5194/essd-2024-115

Saunois, M., Stavert, A. R., Poulter, B., Bousquet, P., Canadell, J. G., Jackson, R. B., et al. (2020). The global methane budget 2000–2017. *Earth System Science Data*, *12*(3), 1561–1623. https://doi.org/10.5194/essd-12-1561-2020

Segers, A., & Nanni, R. (2024). CAMS2_55_CEA – Provision of global inversion-optimised greenhouse gas fluxes and concentrations. Retrieved from https://atmosphere.copernicus.eu/sites/default/files/2024-01/CAMS255_2021SC1_D55.5.2.1-2023-PartCH4_Contribution_to_documentation_of_products_and_services__v1.pdf

Shen, L., Jacob, D. J., Gautam, R., Omara, M., Scarpelli, T. R., Lorente, A., et al. (2023). National quantifications of methane emissions from fuel exploitation using high resolution inversions of satellite observations. *Nature Communications*, *14*(1), 4948. https://doi.org/10.1038/s41467-023-40671-6

Sherwin, E. D., Rutherford, J. S., Zhang, Z., Chen, Y., Wetherley, E. B., Yakovlev, P. V., et al. (2024). US oil and gas system emissions from nearly one million aerial site measurements. *Nature*, *627*(8003), 328–334. https://doi.org/10.1038/s41586-024-07117-5

Shin, H. H., & Hong, S.-Y. (2013). Analysis of resolved and parameterized vertical transports in convective boundary layers at gray-zone resolutions. *Journal of the Atmospheric Sciences*, *70*(10), 3248–3261. https://doi.org/10.1175/JAS-D-12-0290.1

Shin, H. H., & Hong, S. Y. (2015). Representation of the subgrid-scale turbulent transport in convective boundary layers at gray-zone resolutions. *Monthly Weather Review*, *143*(1), 250–271. https://doi.org/10.1175/Mwr-D-14-00116.1

Smagorinsky, J. (1993). *Some historical remarks on the use of nonlinear viscosities* large eddy Simulation of complex Engineering and geophysical flow. Cambridge University Press.

Smith, R. (1979). The influence of the earth's rotation on mountain wave drag. *Journal of the Atmospheric Sciences*, *36*(1), 177–180. https://doi.org/10.1175/1520-0469(1979)036<0177:TIOTER>2.0.CO;2

Stovern, M., Murray, J., Schwartz, C., Beeler, C., & Thoma, E. D. (2020). Understanding oil and gas pneumatic controllers in the Denver–Julesburg basin using optical gas imaging. *Journal of the Air and Waste Management Association*, *70*(4), 468–480. https://doi.org/10.1080/10962247.2020.1735576

Stull, R. B. (1988). *An introduction to boundary layer meteorology*. Springer Netherlands.

Sun, W. Y., & Chang, C. Z. (1986). Diffusion-model for a convective layer .1. Numerical-simulation of convective boundary-layer. *Journal of Climate and Applied Meteorology*, *25*(10), 1445–1453. https://doi.org/10.1175/1520-0450(1986)025<1445:Dmfacl>2.0.Co;2

Taylor, D. M., Chow, F. K., Delkash, M., & Imhoff, P. T. (2016). Numerical simulations to assess the tracer dilution method for measurement of landfill methane emissions. *Waste Management*, *56*, 298–309. https://doi.org/10.1016/j.wasman.2016.06.040

Tibrewal, K., Ciais, P., Saunois, M., Martinez, A., Lin, X., Thanwerdas, J., et al. (2024). Assessment of methane emissions from oil, gas and coal sectors across inventories and atmospheric inversions. *Communications Earth & Environment*, *5*(1), 26. https://doi.org/10.1038/s43247-023-01190-w

Torres, V. M., Sullivan, D. W., He'Bert, E., Spinhirne, J., Modi, M., & Allen, D. T. (2022). Field inter-comparison of low-cost sensors for monitoring methane emissions from oil and gas production operations. *Atmos. Meas. Tech. Discuss.*, *2022*, 1–22. https://doi.org/10.5194/amt-2022-24

USEER. (2023). United States energy and employment report by state: 2023. Retrieved from https://www.energy.gov/sites/default/files/2023-06/2023%20USEER%20States%20Complete.pdf

U.S. EIA. (2023). State energy data system (SEDS). Retrieved from https://www.eia.gov/state/seds/

U.S. EPA. (2014). Leak detection and repair, A best practices guide. Retrieved from https://www.epa.gov/sites/default/files/2014-02/documents/ldarguide.pdf

U.S. EPA. (2014). Other test method (OTM) 33 and 33A GeospatialMea- surement of air pollution-remote emissions quantification- direct assessment (GMAP-REQ-DA). Retrieved from https://www.epa.gov/emc

U.S. EPA. (2017). Method 21 determination of volatile organic compound leaks. Retrieved from https://www.epa.gov/emc/method-21-volatile-organic-compound-leaks

Wang, J. F., Ji, J. W., Ravikumar, A. P., Savarese, S., & Brandt, A. R. (2022). VideoGasNet: Deep learning for natural gas methane leak classification using an infrared camera. *Energy*, *238*, 121516. https://doi.org/10.1016/j.energy.2021.121516

Wang, J. F., Tchapmi, L. P., Ravikumar, A. P., McGuire, M., Bell, C. S., Zimmerle, D., et al. (2020). Machine vision for natural gas methane emissions detection using an infrared camera. *Applied Energy*, *257*, 113998. https://doi.org/10.1016/j.apenergy.2019.113998

Wang, Q., Hu, X.-M., Klein, P. M., Weng, B., Xue, M., Honeycutt, W., & Wang, C. (2024). Examination of meteorological factors and emissions sources leading to the large methane (CH_4) enhancements at the ARM site. In Oklahoma *Paper presented at the AGU annual meeting. D.C.* Retrieved from https://agu.confex.com/agu/agu24/meetingapp.cgi/Paper/1544297

Wyngaard, J. C. (2010). *Turbulence in the atmosphere*. Cambridge University Press.

Wyngaard, J. C., & Coté, O. R. (1974). The evolution of a convective planetary boundary layer—A higher-order-closure model study. *Boundary-Layer Meteorology*, *7*(3), 289–308. https://doi.org/10.1007/bf00240833

Xiao, X. M., Hollinger, D., Aber, J., Goltz, M., Davidson, E. A., Zhang, Q. Y., & Moore, B. (2004). Satellite-based modeling of gross primary production in an evergreen needleleaf forest. *Remote Sensing of Environment*, *89*(4), 519–534. https://doi.org/10.1016/j.rse.2003.11.008

Xue, M., & Thorpe, A. J. (1991). A mesoscale numerical model using the nonhydrostatic pressure-based sigma-coordinate equations: Model experiments with dry mountain flows. *Monthly Weather Review*, *119*(5), 1168–1185. https://doi.org/10.1175/1520-0493(1991)119<1168:AMNMUT>2.0.CO;2

Ye, X., Lauvaux, T., Kort, E. A., Oda, T., Feng, S., Lin, J. C., et al. (2020). Constraining fossil fuel CO2 emissions from urban area using OCO-2 observations of total column CO2. *Journal of Geophysical Research: Atmospheres*, *125*(8), e2019JD030528. https://doi.org/10.1029/2019jd030528

Yu, S. C., Eder, B., Dennis, R., Chu, S. H., & Schwartz, S. E. (2006). New unbiased symmetric metrics for evaluation of air quality models. *Atmospheric Science Letters*, *7*(1), 26–34. https://doi.org/10.1002/asl.125

Zeng, Y., & Morris, J. (2019). Detection limits of optical gas imagers as a function of temperature differential and distance. *Journal of the Air and Waste Management Association*, *69*(3), 351–361. https://doi.org/10.1080/10962247.2018.1540366

Zhang, X., Bao, J.-W., Chen, B., & Grell, E. D. (2018). A three-dimensional scale-adaptive turbulent kinetic energy scheme in the WRF-ARW model. *Monthly Weather Review*, *146*(7), 2023–2045. https://doi.org/10.1175/MWR-D-17-0356.1

Zhao, X., Chen, J., Marshall, J., Gałkowski, M., Hachinger, S., Dietrich, F., et al. (2023). Understanding greenhouse gas (GHG) column concentrations in Munich using the Weather Research and Forecasting (WRF) model. *Atmospheric Chemistry and Physics*, *23*(22), 14325–14347. https://doi.org/10.5194/acp-23-14325-2023

Zhao, X., Marshall, J., Hachinger, S., Gerbig, C., Frey, M., Hase, F., & Chen, J. (2019). Analysis of total column CO2 and CH4 measurements in Berlin with WRF-GHG. *Atmospheric Chemistry and Physics*, *19*(17), 11279–11302. https://doi.org/10.5194/acp-19-11279-2019